Simulating atomic processes in Non-contact Atomic Force Microscopy of ionic surfaces

Filippo Federici Canova

August 21, 2012

Abstract

The Non-contact Atomic Force Microscope (NC-AFM) can nowadays resolve individual atoms on different kind of surfaces. However, in nearly all experiments, the the measured signals are not trivially interpreted and in many cases the origin of the atomically resolved features remains unknown. Comparing experimental images to theoretical predictions, where the atomic structure of the system is known from the beginning, can improve the understanding of the atomic scale processes involved in the imaging mechanism.

We applied available models to study the tip-sample interactions to study different NC-AFM experiments starting from the tip dependent atomically resolved NC-AFM contrast on the $MgAl_2O_4$ spinel surface, where we could establish the atomic structure of the surface termination, the nature of surface defects and the role of adsorbed hydrogen in the experimental images.

Potential variations near a LiF (001) step edge were measured in the torsional channel of the bimodal AFM experiment. Due to the different scales of the interactions involved, a true multiscale model of the system was required to be calculated correctly the displacing effect of the electrostatic field on the undercoordinated atoms at the step edge. The coupling between these two caused a small surface dipole that was the source of the experimental signal.

The well known theory of dynamic response to describe the non-conservative tip-surface interaction and the consequent energy dissipation measurable in NC-AFM experiments, was used on the NaCl (001) surface. Despite the difficulties in finding a good model for the tip, dissipation of the same order as experimentally seen could be simulated. However, in order to provide a full dynamical description of dissipative processes in ionic materials, we implemented a fast molecular dynamics code for graphics processing units, and simulated the experiment starting from the formation of the tip: our results show that the main source of energy dissipation during the tip oscillation is the stochastic formation and rupture of atomic chains diffusing from the tip. The same method was then extended to simulate the bimodal measurements on NaCl:Br flat surface and understand the origin of energy dissipation in the torsional channel, which is associated with frictional properties of the surface. Again, the dissipative processes were revealed and quantitative agreement with the experiment was obtained.

This thesis shows the importance of theoretical modelling in interpreting NC-AFM measurements, making it possible to understand the atomic structure of the imaged surface, its interaction with the tip, and the characteristics of the tip itself that cause the appearance of energy dissipation.

Foreword

This thesis consists of an introductory part and articles published in refereed journals. The first chapter introduces the field atomic force microscopy (AFM), presenting its historical background, the evolution of the field and its broad scientific success. A simple classical model explaining the working principle of non-contact atomic force microscope (NC-AFM) is presented in section 1.2. Amplitude and frequency modulation operation modes are explained in more depth in sections 1.3 and 1.4 respectively, and finally the issue of energy dissipation - one of the main foci of the scientific research proposed in the thesis - is treated in section 1.5. The second chapter presents the theoretical methods employed in our investigations; a considerable amount of effort was put into developing the software such as a flexible, arbitrary setup virtual-AFM (section 2.1) to simulate novel AFM operation modes, and a fast molecular dynamics code (section 2.4.3) to simulate the atomic scale nature of dissipative processes. Chapter 3 will present a summary of the most relevant results from the papers included in this thesis while chapter 4 concludes and summarizes the thesis.

The author wishes to extend his gratitude to all the people who provided him scientific, as well as personal, support during the time spent working on this thesis. Particular thank thanks are due to Adam Foster for constant support, interesting discussion and the wonderful journeys around the world showing our activities to the scientific community; his effort to put the author back on track when lost chasing more elegant mathematics and developing more performing algorithms was very appreciated. Special thanks are due to Teemu Hynninen for useful discussion and pleasant gaming time, and to Bernhard Reischl for sharing his working knowledge of molecular dynamics that made a considerable part of this thesis possible.

List of Publications

The following publications are included in this thesis:

I Filippo Federici Canova and Adam S. Foster, The role of the tip in non-contact atomic force microscopy dissipation images of ionic surfaces, *Nanotechnology*, **22**, 045702 (2011)

II Morten K. Rasmussen, Adam S. Foster, Berit Hinnemann, Filippo Federici Canova, Stig Helveg, Kristoffer Meinander, Natalia M. Martin, Jan Knudsen, Alina Vlad, Edvin Lundgren, Andreas Stierle, Flemming Besenbacher and Jeppe V. Lauritsen, Stable Cation Inversion at the $MgAl_2O_4(100)$ Surface, *Physical Review Letters*, **107**, 036102 (2011)

III Morten K. Rasmussen, Adam S. Foster, Filippo Federici Canova, Berit Hinnemann, Stig Helveg, Kristoffer Meinander, Flemming Besenbacher and Jeppe V. Lauritsen, Noncontact atomic force microscopy imaging of atomic structure and cation defects of the polar $MgAl_2O_4(100)$ surface: Experiments and first-principles simulations, *Physical Review B*, **84**, 235419 (2011)

IV Shigeki Kawai, Filippo Federici Canova, Thilo Glatzel, Adam S. Foster and Ernst Meyer, Atomic-scale dissipation processes in dynamic force spectroscopy, *Physical Review B*, **84**, 115415 (2011)

Articles submitted or in preparation included in this thesis:

V Shigeki Kawai, Filippo Federici Canova, Thilo Glatzel, Teemu Hynninen, Ernst Meyer and Adam S. Foster, Measuring electronic field induced sub-picometer displacement of step edge ions, *Physical Review Letters*, 2012 (submitted)

VI Filippo Federici Canova, Adam S. Foster, Morten K. Rasmussen, Flemming Besenbacher and Jeppe V. Lauritsen, Non-contact atomic force microscopy study of hydroxyl groups on the spinel $MgAl_2O_4(100)$ surface, *Nanotechnology*, 2012 (submitted)

VII Filippo Federici Canova, Shigeki Kawai, Thilo Glatzel, Adam S. Foster and Ernst Meyer, Atomic-scale dynamics of frictional processes, *Physical Review B*, 2012 (in preparation)

The author gave a major contribution in developing the methodologies and carrying out the theoretical calculations for paper I, IV, V and VII as well as in writing the original manuscripts. In paper II, III, and VI the author's contribution was limited to the simulation component of the theoretical work.

During the duration of the post-graduate studies, the author contributed to the following papers not included in this thesis:

- Luigi Sangaletti, *et al.*, Magnetic polaron percolation on a rutile lattice: A geometrical exploration in the limit of low density of magnetic impurities, *Physical Review B*, **80**, 033201 (2009)
- Giovanni Drera, *et al.*, Spectroscopic evidence of in-gap states at the $SrTiO_3/LaAlO_3$ ultrathin interfaces, Applied Physics Letters, **98**, 052907 (2011)

Contents

1

Non Contact Atomic Force Microscopy

1.1 Introduction

The atomic force microscope (AFM) first appeared in 1986 [1], offering a way to characterize samples by measuring their interaction with a probe in proximity to the surface. The probe consists of a sharp tip attached to the lose end of a cantilever; as it interacts with the sample, the force (either attractive or repulsive) felt by the tip causes the cantilever to bend slightly. This small deflection can be detected by the tunnelling current through another probe, as originally proposed by the inventors, or by shining a laser on the back of the cantilever and measuring the position of the reflected beam (figure 1.1). This technique immediately seemed much more attractive than the scanning tunnelling microscope (STM), as it does not put any constraint on the sample and tip material; it is also not restricted to operate in ultra-high vacuum (UHV) like many other surface techniques: the first AFM showed a lateral resolution of roughly 30 Å operating in air. Despite the appealing features, AFM suffered initially from poorer resolution than STM, mainly because the tip is brought into contact with the surface, and the measured interaction results from the chemical forces between all the tip and surface atoms in the contact region, hence the locality of the measurement is lost. Moreover, as the tip scans, it

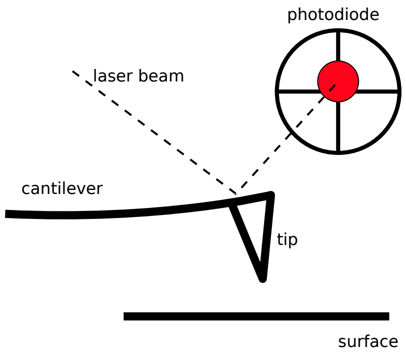

Figure 1.1: Schematic representation of the AFM setup showing the optical lever method for measuring the cantilever deflection.

can suffer damage and degrade, or, if the tip material is hard enough, it can damage the surface itself. Soon after AFM was introduced, several attempts to improve the imaging quality were made, eventually pushing the resolution down to the ångström length scale and beyond. Much better images were obtained with *dynamic* modes, where forces are measured from changes in the dynamical properties of an oscillating cantilever.

The first major improvement to the AFM was introduced in 1987 by Martin and co-workers [2] who proposed to drive the cantilever into a steady oscillation where forces could be deduced from changes in the measured amplitude: for this reason this new mode was called amplitude modulation AFM (AM-AFM). This particular technique proved to be quite successful in imaging soft samples such as biological material, without destroying it, and is still widely used nowadays. Despite the success in proving the concept, AM-AFM presents quite some technical issues. For example, interpreting the measured signal in terms of forces and force gradients becomes quite complicated [3, 4] because the cantilever sweeps quite a wide range of heights during the oscillation cycle, and the tip crosses regions with attractive interactions, down to the contact regime characterised by repulsive forces: in general, only a qualitative analysis is possible. For the same reason, stability in the oscillation becomes a concern, and care must be taken in order to prevent the tip from jumping into contact on the surface. Furthermore, this mode cannot work in UHV environment as explained in more depth in section 1.2 and 1.3, where the AM-AFM theoretical model and experimental apparatus will be presented.

After few years, a different setup was proposed [5] in order to overcome the issues of AM-AFM, where tip-surface interactions were measured from changes in the cantilever's oscillation frequency. The new frequency modulation (FM-AFM) mode could operate in UHV and the first atomically resolved images of semiconducting [6] as well as insulating surface [7, 8] were obtained; dynamic processes such as diffusion of single atoms and defects were also observed [9]. Atomic resolution was also achieved in liquid [10, 11], making it possible to probe the interface between a surface and water [12, 13] and biological samples in their natural environment [14]. FM-AFM is nowadays the preferred mode for high resolution studies, as it usually provides greater sensitivity and more stable operation than AM-AFM: with this setup, a signal can be obtained by oscillating the cantilever further away from the surface, exclusively in the attractive force regime, reducing the risks of jump into contact, and at smaller amplitude, thus enhancing sensitivity. For this reasons interpreting the measured frequency shift and relating it to forces, is easier than AM-AFM and several methods have been developed [15, 16, 17], depending on the approximation made on the cantilever's oscillation and force profiles.

The frequency modulation mode is now just a part of a much wider category of scanning probe techniques called non-contact AFM (NC-AFM), which takes

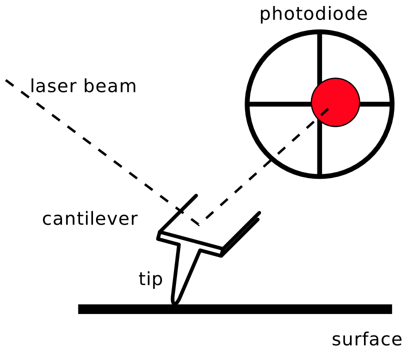

Figure 1.2: Schematic representation of the LFM setup: lateral forces are detected by the torsional twisting of the cantilever.

its name from their common feature: the tip is always sufficiently far from the surface, where the tip-sample force is attractive. The popularity of this mode comes also from the wide range of modifications developed that enables measurement of different surface properties, with the advantage of atomic resolution. Important examples are magnetic force microscopy (MFM) [18] where the tip detects exchange interactions with a magnetic sample, or Kelvin probe force microscopy (KPFM) [19, 20, 21], where the contact potential difference between the tip and the surface is measured, giving a map of the work function at different positions on the sample; NC-AFM can also be combined with STM, measuring simultaneously the electronic and atomic structure of the surface.

An important modification to the AFM has been developed in order to probe lateral forces as well. In the static mode, this can be achieved by scanning in the direction orthogonal to the cantilever main axis and measuring its torsional twist, instead of the flexural bending [22], as illustrated in figure 1.2: the apparatus is known as lateral force microscope (LFM). With this instrument, a researcher could investigate the atomic scale nature of frictional processes [23, 24, 25, 26], providing a better understanding of friction and its origins beyond the empirical laws of classical physics; wear mechanisms of surfaces sliding against a nano-asperity were also studied extensively [27, 28, 29], gaining valuable insight into those processes that lead to mechanical failure in every kind of machinery.

Just like AFM, LFM has a dynamic counterpart as well, where the torsional oscillation of the cantilever is actuated [30, 31] and lateral forces can be calculated from the measured torsional frequency shifts: this mode is called torsional resonance (TR-AFM). This mode is easily combined with the conventional NC-AFM to achieve the so called bimodal AFM [32], that can simultaneously measure normal and lateral forces, providing a more complete map of the interaction potential of any given surface.

NC-AFM is nowadays a widely used characterisation technique and atomic resolution is routinely achieved; for this reason, and due to it flexibility regard-

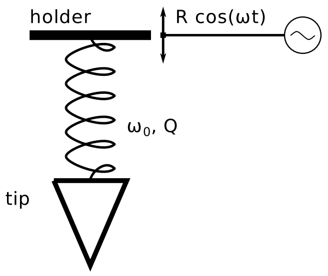

Figure 1.3: Harmonic model for the cantilever.

ing the nature of the sample and imaging environment, NC-AFM was rapidly developed and became a fundamental instrument in very different research fields. In the following sections, a more detailed description of the dynamic mode mechanism, as well as the working principles of AM- and FM-AFM, will be presented as part of this thesis involved developing and operating a virtual simulation of the experimental apparatus. Finally in section 1.5 the issue of energy dissipation will be addressed, giving a thorough explanation of the phenomena and previous research efforts in the field.

1.2 Harmonic Oscillator Model

A simple and successful model for NC-AFM is available from the theory of the harmonic oscillator; if we represent the whole cantilever-tip assembly as a linear spring with a damping and driving excitation (figure 1.3), we can use the well known equations from classical mechanics to describe the vertical position of the tip:

$$\ddot{z}(t) + \frac{\omega_0}{Q}\dot{z}(t) + \omega_0^2 z(t) = R\cos(\omega t) \tag{1.1}$$

where ω_0 is the resonant frequency of the spring, Q its Q-factor and R and ω are the driving amplitude and frequency respectively. The steady state solution of equation 1.1 is an harmonic oscillation:

$$z(t) = A_0\cos(\omega t + \phi) \tag{1.2}$$

with the same frequency as the exciting signal. Its amplitude A_0 and phase ϕ are given by:

$$A_0 = \frac{RQ}{\sqrt{\omega^2\omega_0^2 + Q^2\left(\omega_0^2 - \omega^2\right)^2}} \quad \text{and} \quad \phi = arctan\left(\frac{\omega\omega_0}{Q\left(\omega_0^2 - \omega^2\right)}\right) \tag{1.3}$$

The oscillator reaches the steady state with a characteristic decay time $\tau = 2Q/\omega_0$ and this can be quite problematic, because for a typical AFM in UHV the Q-factor is as high as 10000 and the frequency around 100 kHz, giving a

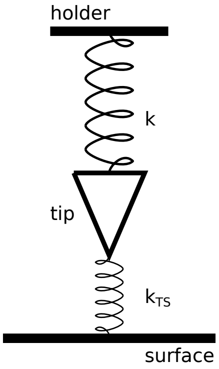

Figure 1.4: Model of the AFM tip including the surface interaction. The cantilever is modelled as a constant spring of stiffness k, while the interaction with the surface is represented by a spring with stiffness k_{TS}, that depends on the actual tip position.

τ of 32 ms. By itself, this fact would make the imaging time utterly large, and combined with thermal drift, imaging would actually be impossible. A way to avoid this issue was developed and it will be presented in section 1.4. For a system with low Q-factor, such as AFM in air or liquid environment, the response is quite fast, and the cantilever can be assumed to be always oscillating at the driving frequency.

So far we did not yet consider the effect of the tip-sample interaction on the oscillation properties. The simplest way to include it, is to model the tip-sample force as a spring with an effective stiffness (figure 1.4):

$$k_{TS} = -\frac{\partial F_{TS}}{\partial z} \tag{1.4}$$

where F_{TS} is the tip-sample force. Thus the resonant frequency of a cantilever having effective mass m^* becomes:

$$\omega^2 = (\omega_0 + \Delta\omega)^2 = \left(k - \frac{\partial F_{TS}}{\partial z}\right)/m^* \tag{1.5}$$

where m^* is the effective mass of the system and k is the spring constant of the cantilever. If $\Delta\omega \ll \omega_0$ we obtain:

$$\Delta\omega = -\frac{\omega_0}{2k} \cdot \frac{\partial F_{TS}}{\partial z} \tag{1.6}$$

According to the model, an external interaction causes the resonant frequency of the cantilever to change proportionally to the gradient of the tip-sample force, and this approximation works remarkably well when the oscillation amplitude is sufficiently small that the force gradient $\partial F_{TS}/\partial z$ does not change significantly during the oscillation cycle. If this condition cannot be satisfied, one needs to take into account the whole profile of the force felt by the tip.

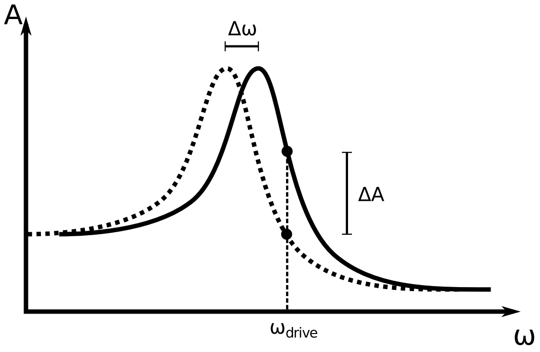

Figure 1.5: Amplitude response calculated from equation 1.3. When the interaction changes the resonant frequency, the peak shifts resulting in an amplitude change.

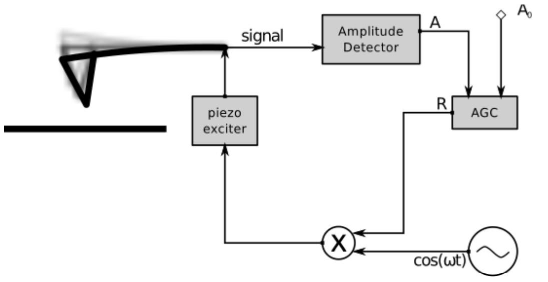

Figure 1.6: Schematic view of the AM-AFM electronics.

1.3 Amplitude Modulation

To better understand dynamic modes, and in particular why FM-AFM is the preferred one, we will explain briefly how AM-AFM works, as it was the first dynamic mode to be invented, and many design concepts are still employed in modern operation modes.

We know from equation 1.6 that the cantilever resonant frequency is affected by tip-sample interactions, but in AM-AFM, changes in frequency cannot be detected directly, because the cantilever is oscillating at the driving frequency ω_{drive}. Despite being undetected, the interaction does change the resonant frequency, and the response curve of the oscillator shifts by a certain $\Delta\omega$, as illustrated in Fig.1.5: at this point the amplitude drops by ΔA. Since changes in amplitude are not advisable (a different amplitude implies a different tip-sample distance and thus a different interaction), a feedback system called automatic gain control (AGC) tunes the intensity of the driving signal, feeding to the cantilever more (or less) energy, until its amplitude reaches again the set-point value A_0 (see figure 1.6). The output signal from the AGC, R, is related to $\Delta\omega$ and thus to the forces we were initially interested in measuring.

This setup works well if the cantilever is always oscillating at the driving

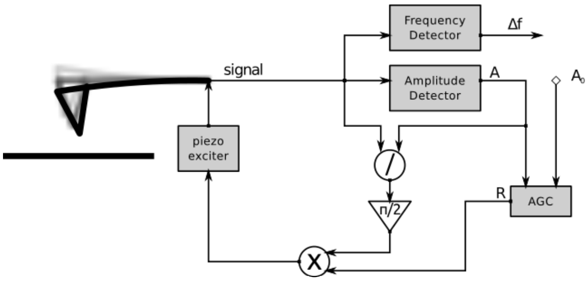

Figure 1.7: Illustration of the FM-AFM self-excitation scheme.

frequency, and this is the case only when the Q factor is small, i.e. when the AFM is in air or liquid environment. Unfortunately, having a clean and neat operation environment such as UHV, helps a lot in achieving atomic resolution, and there, without the friction induced by a medium, Q factors typically go beyond 10000.

1.4 Frequency Modulation

When the Q factor is high, the oscillation frequency decays too slowly towards the driving one, and the AM-AFM scheme is no longer feasible; in such conditions, it is more efficient to tune the driving frequency itself whenever the tip-sample interaction changes the cantilever's frequency. The idea is to always excite the cantilever at its *actual* resonant frequency and the most straightforward way to do it is by using the oscillation signal itself as driving wave, as illustrated in figure 1.7. The oscillation signal is normalised (divided by its amplitude), phase-shifted by $\pi/2$, and finally multiplied by the excitation amplitude R calculated by the AGC. Different methods can be applied to measure the frequency, but most commonly this is done with a circuit called phase-locked-loop (PLL). The PLL measures the phase mismatch between the signal and a reference oscillation provided by an internal voltage controlled oscillator (VCO), and uses it to regulate the frequency of the VCO itself; in some cases, the reference provided by the PLL is used as excitation instead of the cantilever's own signal. Other methods to measure the oscillation frequency, such as Fourier or wavelet decomposition [33] or symmetric quadrature demodulation [34] were developed as well, although they are less frequently employed.

The measured frequency shift Δf contains information about the tip-sample interaction; in case of small amplitude, equation 1.5 provides the connection, otherwise the frequency shift can be obtained assuming the cantilever to be an harmonic oscillator perturbed by a force $F(z)$ [15]:

$$\Delta\omega = -\frac{\omega_0}{k} A_0^2 \left\langle F(z) \right\rangle \tag{1.7}$$

leading to the general relation:

$$\Delta\omega = -\frac{\omega_0}{\pi A_0 k}\int_{-1}^{1} F(d + A_0(1+u))\frac{u}{\sqrt{1-u^2}}du \tag{1.8}$$

where d is the closest approach distance, and A_0 the oscillation amplitude. If the force can be expressed as a simple power law, $F(z) = -Cz^{-n}$, where C is a constant, then expression 1.7 becomes:

$$\Delta\omega = -\frac{\omega_0 C}{2\pi k A_0 d^n}\int_{0}^{2\pi}\frac{\cos x dx}{\left(1+\frac{A_0}{d}(cosx+1)\right)^n} \tag{1.9}$$

An equivalent expression can be obtained considering the Fourier expansion of the cantilever motion [35, 36] as well. A more novel approach consists of integrating the equation of motion of the cantilever subject to the tip-sample interaction and the effect of the different feedback loops (AGC, PLL, ...) modelled around the real experimental apparatus [37]. Since part of this thesis involved development and application of such a method, more details will be given in section 2.1.

From the theoretical point of view, equation 1.8 is enough to calculate a NC-AFM image starting from the tip-sample interaction $F(z)$ obtained from a model, but it does not help much the interpretation of the experiments. In principle, equation 1.8 should be inverted so that the tip-sample interaction can be calculated from the measured frequency shift but no analytical solution can be found for the general case. Numerical schemes were developed to iterate the general solution of equation 1.8 starting from an approximate large amplitude solution [38] and to invert the frequency-force relation numerically using a quadrature scheme [39]. A more recent method was developed [40] to invert the relation analytically: despite being generally valid with respect to the nature of the tip-sample interaction and the oscillation amplitude, in order to be computable the series of functions involved in the treatment have to be truncated and approximated, thus introducing an error in the extracted forces.

1.5 Energy Dissipation

According to expression 1.3, the cantilever's amplitude is proportional to the amplitude of the excitation signal R; when considering FM-AFM, where the oscillation amplitude usually has to be constant, and the system is driven always at its actual resonant frequency, it is clear that the excitation amplitude R should also be constant. If we think about the excitation amplitude as a measure of the energy that is fed into the oscillator [36] in order to compensate for energy losses, the only loss is due to the internal friction of the cantilever, or its friction with the environment, and both contributions do not depend

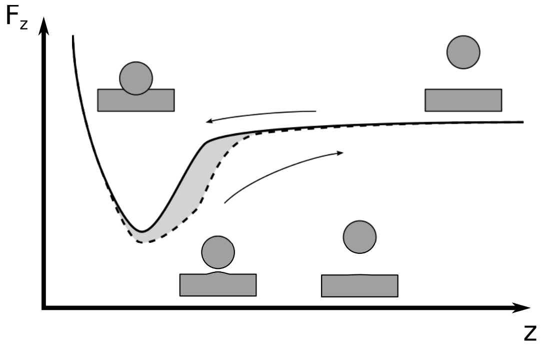

Figure 1.8: Example force curves for approach (solid line) and retraction (dashed line) sweeps, illustrating the adhesion mechanism.

on time, or the particular cantilever position above the surface. Despite this, it is often experimentally observed that R depends on the scanning position, sometimes revealing an atomically resolved pattern that can show features different from the ones seen in topography or Δf maps [41]. This dissipation or damping signal has been observed for a wide variety of different surfaces, including metals [42, 43, 44], semimetals [37, 45, 46], semiconductors [47, 48], insulators [49, 50, 51] and insulating thin films [52, 53, 54, 55]. This suggest the existence of an energy loss mechanism involving the tip and surface atoms [56, 57], although the details of this process are not always well understood. It has even been argued whether damping images are just an artificial result of the complicated electronic devices operating the microscope [58, 59], affecting its measurements with their finite response time, however, various models for non-conservative interactions have been developed and applied in NC-AFM simulation, giving damping values comparable to experiments [60].

The general idea about the dissipation mechanism is that the tip acts as a hammer *hitting* the surface, which takes its time to respond. Therefore, during the retraction part of the oscillation, the tip feels a different force than during the approach phase, causing a small hysteresis to appear (Fig.1.8). Using statistical mechanics Kantorovich [61] showed that stochastic friction causes a small delay in the surface atoms displacement, and hysteresis in the oscillation cycle appears. This model successfully explained how surface atoms attracted to the tip should appear brighter than repelled ones in dissipation images, providing an interesting insight into the contrast mechanism, but the predicted dissipation was several orders of magnitude smaller than typical experimental values, indicating that more dramatic changes must be occurring at the atomic level. Later, Kantorovich and Trevethan [62] proposed a general model, suggesting that larger hysteresis can be seen when surface atoms exhibit a bistable behaviour in presence of the AFM probe (more details in section 2.3), and proved its applicability to ionic crystals. Reversible reconstructions induced by the tip have also been calculated for different kind of systems; in Ref.[63] small displacements of inversion defects in III-V (110) surface were found to be responsible for NC-AFM energy dissipation, and while these defects did not appear clearly in the topography, they gave a clear signature in the dissipation maps. Dissipation processes have also been thoroughly studied on the Ge (111) surface [47], where a surface adatom was predicted to break and reform its bond with the surface as a result of the tip approach and retraction: the calculated hysteresis was also in good agreement with the measured quantity. Hysteresis coming from bistability of surface atoms was also predicted for metal samples [42, 44, 43].

Despite all the above mentioned studies providing a good description of the experimental observations in terms of surface processes, it is often seen that the particular tip used as a trigger for those processes plays a major role in dissipation. A dissipative process on the very same surface can be enhanced, or impeded, if only few atoms in the tip apex change position [64]. This is particularly bad, because the tip cannot be easily controlled and its atomic scale structure is, in most cases, unknown; it is often observed in experiments, that the imaging contrast changes while scanning, as a result of small structural changes or adsorption of surface atoms at the tip apex. Furthermore, dissipation is not always a surface process: reversible changes can happen mainly in the tip, giving a different interaction during approach and retraction, and the surface just acts as trigger. Dissipative mechanisms in Si surface were extensively studied in Ref.[65], where several low energy Si tip configurations were considered as AFM probes. Statistical jumps between the possible tips, induced by proximity to the surface, gave enough hysteresis in the oscillation cycle to be considered the main dissipative process in the system. In Ref.[66] reversible but hysteretic configuration jumps in both surface and tip atoms were found to be responsible for energy dissipation and their dependence on tip position and distance to the surface, as well as spin polarization were calculated.

Our efforts first focused on characterizing the tip's properties that activate dissipative processes on ionic crystal surfaces [64], using the quasi-static approach described in Ref.[62], and explained in more details in section 2.3.

A considerable effort was made in this thesis to give a better understanding of NC-AFM energy dissipation mechanisms and aid, with the guide of theoretical calculation, interpretation of experimental observations.

2

Simulation Methods

2.1 Virtual AFM

The analytical expressions 1.6 and 1.9 allow us to calculate the expected frequency shift out of a forcefield: after calculating the tip-sample interaction with some theoretical model, we can predict what the experimental Δf image would look like, eventually understanding the relationship between image features and the real physics of the system. However, those expressions do not take into account energy dissipation, and can only be applied within the approximations that were made (small amplitude, harmonic oscillation, ...); the complicated nature of the experimental setup is also left out, together with all possible artefacts they might induce on the measurements. It would be more desirable to have a NC-AFM model with the least approximations, reproducing the behaviour of the whole apparatus: a virtual-AFM.

The virtual-AFM [37] integrates the cantilever's dynamics taking into account the tip-sample interaction $\vec{F}_{TS}$ and the response of the different feedback circuits, in the discretised time-domain. If the cantilever-tip assembly is represented by an harmonic oscillator, then for bimodal mode the vertical and lateral position of the tip are given by:

$$\begin{aligned} \ddot{z} + \omega_{0z}^2(z - z_0) - \frac{\omega_{0z}}{Q_z}\dot{z} &= R_z(t)E_z(t) + F_z^{TS}(x, y, z) \\ \ddot{y} + \omega_{0y}^2(y - y_0) - \frac{\omega_{0y}}{Q_y}\dot{y} &= R_y(t)E_y(t) + F_y^{TS}(x, y, z) \end{aligned} \tag{2.1}$$

where ω_0 are the resonant frequencies and Q the Q-factors of the flexural and torsional springs, while z_0 and y_0 describe the position of the fixed end of the cantilever that can be controlled to approach and scan the surface; in our case, the tip-sample force $\vec{F}_{TS}$ is calculated with a classical atomistic model of the system under study. The excitation amplitudes $R(t)$ and signals $E(t)$ are given by the feedback circuits: since these depend on the cantilever oscillation properties (amplitude, phase and frequency) they introduce an explicit time dependence into the equation, which cannot be solved analytically any

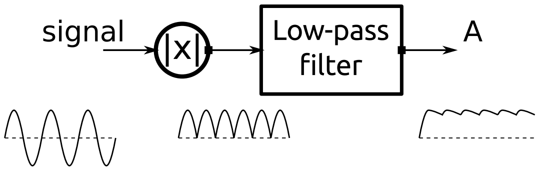

Figure 2.1: Schematics of the amplitude demodulator. The wave forms illustrate the signal processing at each step.

more. Furthermore, the particular choice of circuits depend on the particular experimental setup, often tuned for a very specific application. For these reasons, we developed an arbitrary setup virtual-AFM, implementing only the behaviour of elementary circuits such as oscillators, filters, arithmetical/logical operators and simple controllers: this way the program is not tied to one specific operation mode of one specific instrument.

One of the key components in any NC-AFM apparatus are low-pass filters; differently from the previous implementation in Ref.[67], our low-pass filters are based on the Sallen-Key topology, which is modelled by the transfer function of the ideal circuit:

$$y(s) = G\frac{x(s)}{s^2 + \frac{\omega_c}{Q}s + \omega_c^2} \tag{2.2}$$

where $x(s)$ and $y(s)$ are the input and output signal respectively, G is the gain, Q the quality factor, and ω_c the cutoff frequency. The filter is tuned to behave as a second order Butterworth filter by choosing $G = 1.5708$ and $Q = 0.7071$. The transfer function, expressed in the frequency-domain, is converted into the time-domain with a Laplace transform, and then discretised, so that at any simulation step the output of the filter can be calculated from the input and output values in the preceding two steps.

The amplitude demodulator is implemented as a series of circuits shown in figure 2.1. First the absolute value of the input signal is calculated, and then fed to a low-pass filter with the cutoff frequency determined by the measurement bandwidth. The AGC is implemented as a proportional-integral controller that compares the measured amplitude to a set-point value and gives an output $R(t)$ as follows:

$$R(t) = K_p\left(A_0 - A(t)\right) + K_i\int_0^t \left(A_0 - A(\tau)\right)d\tau \tag{2.3}$$

where A_0 is the set-point and K_p and K_i are the proportional and integral constant respectively. These constants are chosen to be stiff enough for the AGC to respond quickly to changes in amplitude, without inducing artificial oscillations in the output. The output signal $R(t)$ will be used as amplitude for the excitation signal.

An analog PLL circuit, shown in figure 2.2, was assembled from elementary components as well. First, the cantilever's signal and the reference oscillation

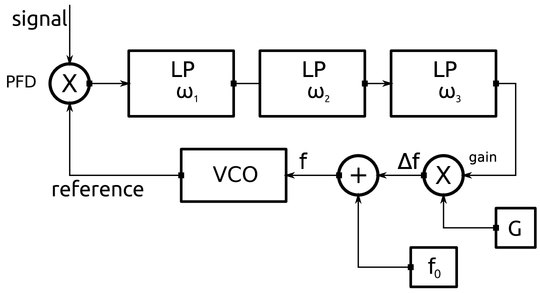

Figure 2.2: Example of the analog PLL circuit.

coming from the voltage controlled oscillator (VCO) are multiplied together by the phase-frequency detector (PFD). The resulting waveform is processed by a series of three low-pass filters with decreasing cutoff frequencies, providing an estimate of the phase mismatch between the two oscillations. The mismatch is then amplified by a constant gain and used as frequency shift to tune the frequency of the VCO itself; an alternative implementation replaces the constant gain with a PI controller representing the charge pump. Note that this circuit is the main source of numerical error due to the discrete time-step. When the signal and reference are multiplied in the PFD, the output wave contains a high frequency component at about $2f$, and even if the time-step is chosen to integrate correctly the cantilever's trajectory, it might not be small enough to sample correctly higher frequencies. The error therefore propagates through the filters and induces an offset of a few Hz in the measured frequency shift, but it can be reduced by making the time-step smaller, thus increasing the computational time. We were also able to implement a digital PLL to avoid this issue.

2.2 Tip-Surface Interactions

After the virtual-AFM is configured to simulate an experiment, we need to provide a description of the tip-sample interactions $\vec{F}_{TS}$ (forcefield), and possibly of the non-conservative effects as well (dissipative field). The general way to proceed is by cutting a slab of the surface material under study, and use it as surface model; the slab should be thick and wide enough so that the calculation is not affected by the finite size. Slab atoms in the lower atomic layer should be frozen, or restrained, in the predicted bulk positions to prevent the slab from drifting towards the tip. Since in the experiments, the tip is often indented in the sample beforehand, in order to enhance imaging resolution, it is quite fair to assume the apex of the tip to be covered with surface material; thus the tip can be modelled as a small cluster of surface material exposing a sharp corner towards the surface. The topmost atoms of the tip have to be constrained, as they represent the macroscopic part of the tip-cantilever assembly externally

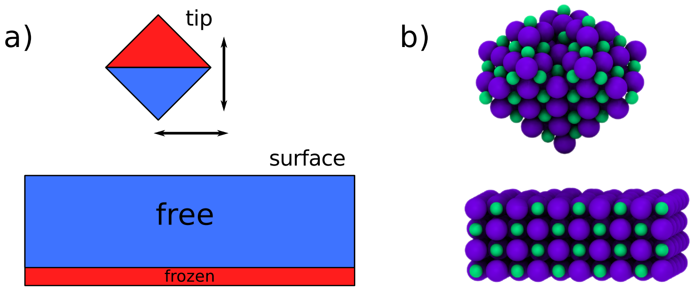

Figure 2.3: (a) Illustration of the tip and surface model used for NC-AFM simulation, with their frozen boundary layers (red regions) and free parts (blue regions). The forcefield is obtained by calculating the total force on the tip for a set of tip's positions in the volume of space above the surface.

controlled during the experiment; a schematic representation of the model is showed in figure 2.3a, along with a real example for NaCl (001) flat surface in figure 2.3b. The tip-sample distance is defined as the distance between a fixed *marker* point attached to the tip, possibly in the position of the foremost apex atom, and the theoretical height of the surface atomic layer.

The tip-sample forcefield is then obtained by placing the tip in certain positions above the surface, calculating the total force acting on it for each point. The atomic and electronic coordinates have to be relaxed each time, making sure the system is in its ground-state: it is important to capture the relaxation of the tip apex in close approach to the surface, as this can have remarkable influence on the simulated images. The easiest way to proceed, is to construct a regular volumetric grid in the region of interest and repeat the calculation with the tip placed on the grid points, while forces everywhere else can be linearly interpolated by the virtual-AFM, although this might be computationally too expensive for quantum mechanical models. In such case, it is more convenient to compute tip-sample forces on a few relevant points of the surface, typically on surface atomic sites and in between, for different tip heights; the calculated force curves then need to be interpolated with a more advanced method that allows sparse data grids. It is also possible to simulate KPFM images by calculating the forcefield also depending on the bias voltage applied between the tip and the surface: this requires much more intensive computation and proper care has to be taken in order to account for the macroscopic tip-sample electrostatic field.

Since the tip-sample force will be evaluated at every time-step in the virtual-AFM, the preferred interpolation method is multi-linear, as it is the simplest; it is important that the data grid is fine enough to give a smooth interpolation throughout the cantilever oscillation cycle, because the resulting frequency shift is sensitive to the gradient of the force. Other interpolation schemes providing smooth interpolation with fewer data points were developed, although they

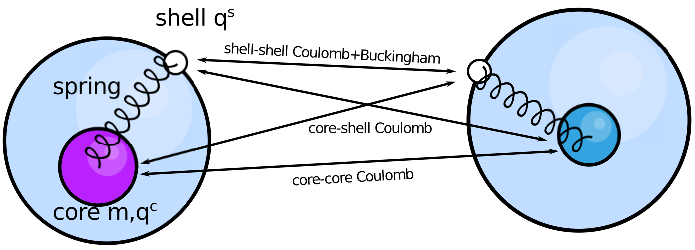

Figure 2.4: Interatomic interactions within the shell model.

should not be trusted to produce features with higher resolution than the data grid.

The choice of model for interatomic interactions is usually dictated by the materials involved, the level of accuracy required, and the computational cost of the model itself, as long as the processes thought to be responsible for the NC-AFM imaging mechanism are accounted for. In our work, we used classical models to describe the simple ionic crystal surfaces [68, 69], and quantum density functional theory (DFT) [70] where the surface under study required a full description of the electrons. These methods will be presented in the following sections.

2.2.1 Classical Interaction Model

Ionic crystals such as NaCl can be fairly accurately described using classical models, where the chemical bonds are described with analytical formulae. In our studies we used the shell model [68], in which atoms consist of a massive positive point charge q^c representing the core, and a negative point charge q^s for the electronic shell: core and shell charge within the same atom only interact through a linear spring, emulating the atomic polarisation. Different atoms interact through Coulomb electrostatic forces between all their charges, and short-range chemical interactions, described by Buckingham pair-wise potentials [69] are added to the shells, as shown in figure 2.4. Short-range potentials are given by:

$$V = A_{ij} \exp^{-\frac{r_{ij}}{\rho_{ij}}} + \frac{B_{ij}}{r_{ij}^6} \tag{2.4}$$

where r_{ij} is the distance between two shells and the parameters A_{ij}, B_{ij} and ρ_{ij} define the interaction between the two atomic species; parameters for our materials of interest can be found in Ref.[71]. In order to find the ground state of the system, first the positions of the shells are optimised with the cores fixed; then the forces on the atoms are evaluated again (without the polarization spring contribution) and displaced accordingly to reach a lower energy configuration. The procedure is repeated until a convergence criteria is met.

2.2.2 Quantum Density Functional Theory

In some cases, a classical description of the system is bound to fail, because the effects of the electronic processes cannot be efficiently approximated with analytical expressions. Density Functional Theory (DFT) is one of many ab initio techniques which attempt to solve the many-body Schrödinger equation:

$$H\Psi_i(1,2,...N) = E_i\Psi_i(1,2,...N) \tag{2.5}$$

where H is the Hamiltonian of a quantum mechanical system composed of N particles, Ψ_i is its ith wavefunction and E_i is the energy eigenvalue of the ith state. The particle coordinates $(1,2,...N)$ are usually referring to their spin state and position. For electronic systems with non-relativistic velocities the Hamiltonian for an N-electron system is:

$$H = -\frac{1}{2}\sum_{i=1}^{N}\nabla_i^2 + \sum_{i>j}^{N}\frac{1}{|\vec{r}_i - \vec{r}_j|}...... + \sum_{i=1}^{N}V_{Ne}(\vec{r}_i) \tag{2.6}$$

where the first term represents the electron kinetic energy, the second term the electron-electron Coulomb interactions and the third term is the coulomb potential generated by the nuclei; this equation also assumes that the nuclei are effectively stationary with respect to electron motion (Born-Oppenheimer approximation). Since every electron has 3 spatial degrees of freedom, this is effectively a $3N$ dimensional problem and in almost all interesting cases, it is too complicated to be solved even numerically and further approximations need to be made.

Since it has been demonstrated that the ground state properties of a many-electron system are uniquely determined by an electron density $\rho(\vec{r})$ that depends on only 3 spatial coordinates, it is possible to reformulate Schrödinger equation in terms of the density and reduce considerably the dimensionality of the problem [72]. The kinetic energy and the electron-electron interaction are described by a universal functional $F[\rho(\vec{r})]$ of the electron charge density and the total energy of the electronic system can be written as:

$$E = \int V_{Ne}(\vec{r})\rho(\vec{r})d\vec{r} + F[\rho(\vec{r})] \tag{2.7}$$

The ground state of the system is found by minimising expression 2.7 with respect to the density. This in principle gives the exact solution to the initial problem if the functional $F[\rho(\vec{r})]$ is known. Unfortunately, its exact form has not been found, so approximations must be used to describe the exchange and correlation energies coming from the electron-electron interaction [70, 73, 74, 75, 76, 77]. However, DFT is preferred over higher order ab initio methods due to its lower computational cost, enabling calculation of systems up to tens of thousands atoms [78].

2.3 Dissipative Field

The forcefield describes how the tip interacts with the surface but there is no difference between the approach and retraction sweeps, thus it does not contain hysteretic effects: it is conservative. Non-conservative effects can be included using the theory of dynamic response [62] where the presence of the tip above the surface creates a secondary stable configuration for the system, obtained by displacing a surface atom from the ground state position towards the tip: the continuous hopping between the two stable states results in the adhesion mechanism responsible for energy dissipation. Once the stable configurations, namely A and B, and the transition state T in between have been identified, we can calculate the transition rates W_{AB} and W_{BA}, as well as the forces acting on the tip in both cases, F_A and F_B. The transition rates are given by:

$$W_{AB} = \nu_A exp\left(-\frac{E_{TA}}{k_B T}\right) \tag{2.8}$$

where ν_A is the attempt frequency calculated from the curvature of the minimum A, $E_{TA} = E_T - E_A$ is the energy barrier to overcome, k_B the Boltzmann constant and T the temperature. The reverse process transition rate W_{BA} has an analogous expression. All these information build a secondary data grid called *dissipative field* that will be used by the virtual-AFM to integrate the probability for the system to be in the state A:

$$\frac{dP_A}{dt} = -P_A W_{AB} + P_B W_{BA} \tag{2.9}$$

where $P_B = 1 - P_A$. The transition rates depend on the position of the tip and the total tip-surface interaction becomes:

$$\vec{F}(x, y, z) = P_A \vec{F}_A(x, y, z) + P_B \vec{F}_B(x, y, z) \tag{2.10}$$

This approach is in principle general, but in order to obtain a dissipative field we need to have an idea of what the process can be. Short molecular dynamics simulations in Ref.[62], showed how a surface atom attracted by the tip exhibited the tendency to oscillate towards the apex and this was thought to be the dissipative mechanism. In our calculations, we identify the surface atom mostly affected by the tip - either though intuition or via running short molecular dynamics. Then we displace it gradually towards the tip and compute the total energy of the system at each step (figure 2.5). Only the vertical coordinate q_z of the jumping atom is constrained and the atom is free to move within the xy plane, and the rest of the system is allowed to relax.

The virtual-AFM will integrate the statistical behaviour of the system from equation 2.9 along with the oscillation of the cantilever, and the tip-sample force will be given by 2.10, hopefully showing a difference in approach and retraction.

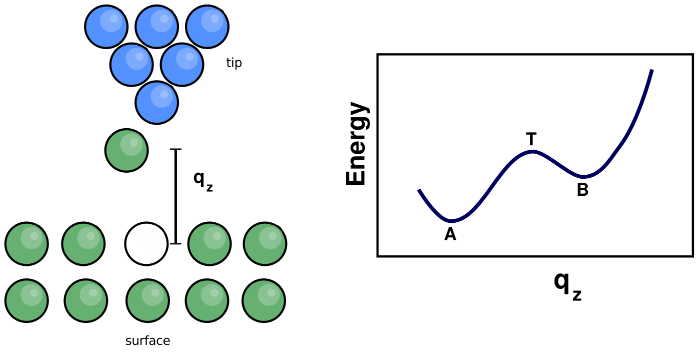

Figure 2.5: Surface atom displacement q_z and corresponding energy of the system.

2.4 Dynamic Methods

According to Ref.[62], the source of NC-AFM energy dissipation in ionic crystals is the instability of the surface in the presence of the tip, as suggested by observation of short molecular dynamics (MD) trajectories. Due to the limitations of computational resources at the time, only few picoseconds trajectories could be simulated with MD, and since this is about seven orders of magnitude smaller than the duration of a NC-AFM oscillation cycle, other dissipative processes with longer characteristic time-scale, do not appear in the simulation. Considerable effort was made, in the course of this thesis, to push the limitation of MD simulation towards longer trajectories, looking for a full dynamical description of the dissipative processes.

The main goal is to simulate the behaviour of the tip and surface atoms as the tip oscillates; the total force $\vec{F}_{TS}(\vec{x}_{tip})$ acting on the tip can be recorded as a function of its position $\vec{x}_{tip}$, and the hysteresis is given by:

$$E = \oint_{\gamma} \vec{F}_{TS}(\vec{x}) \cdot d\vec{x} \tag{2.11}$$

where the integration covers the whole loop γ. This provides a measure of the energy lost during one cycle, under the assumption that the oscillation is harmonic, i.e. the effect of the energy loss on a single oscillation is negligible: the approximation is good because for a typical cantilever oscillating with 1 nm amplitude, an energy dissipation of 0.5 eV/cycle causes an amplitude drop of 4 pm, which is less than 1%, meaning that the oscillation can be assumed to be harmonic.

In the following section we will give a brief introduction to MD, pointing out its issues and in section 2.4.3 our solutions will be explained.

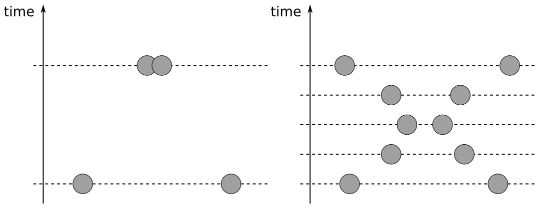

Figure 2.6: Illustration of MD discrete integration. If the time-step is too large the numerical solution is wrong.

2.4.1 Molecular Dynamics

In many cases it might be interesting to see how material properties arise from the atomic scale dynamical behaviour of the system: molecular dynamics is a conceptually simple method to calculate such behaviour. The main idea is to integrate the complex equations of motion for a many-body system, and calculate the trajectory of each particle in the system; in principle, for any system consisting of N particles, we want to solve these linear differential equations:

$$m_i \frac{d^2\vec{x}_i(t)}{dt^2} = \sum_{j\neq i}^{N} \vec{F}_{ij}\left(\vec{x}_i - \vec{x}_j\right) \quad i = 1, 2, ..., N \tag{2.12}$$

where m_i is the particle mass, $\vec{x}_i(t)$ its position at any time t, and $\vec{F}_{ij}$ is the force acting on particle i due to its interaction with particle j; the interaction between two particles, at a given time, is assumed to depend only on their positions at the same time. The only way to solve such complicated system, is by discretising time and integrating the equations 2.12 step by step, starting from a set of initial conditions for positions $\vec{x}_i(0)$ and velocities $\vec{v}_i(0)$. Having a discrete time-step already introduces an integration error, and since the equation will be integrated step by step, the error accumulates throughout the calculation if proper care is not taken. If the time-step is too large it can (and most likely will) happen that two particles approaching each other, will become closer than they should, and the steric repulsion will accelerate them too much (figure 2.6), ultimately exploding the system. Therefore, the time-step should be smaller than the characteristic time of the fastest degree of freedom in the system, but a too small time-step will also fail because computers represent numbers with finite precision: a quite standard choice for the time-step is 1 fs. Moreover, the particular algorithm chosen also matters because the result of a computer calculation is also sensitive to the particular execution order of the instructions: despite that the problem is conceptually simple, solving *correctly* equation 2.12 with a computer can be a quite difficult task.

The algorithm of our choice to integrate atomic trajectories is called *leapfrog* and, for every particle i, its position and velocities in the k-th time-step can

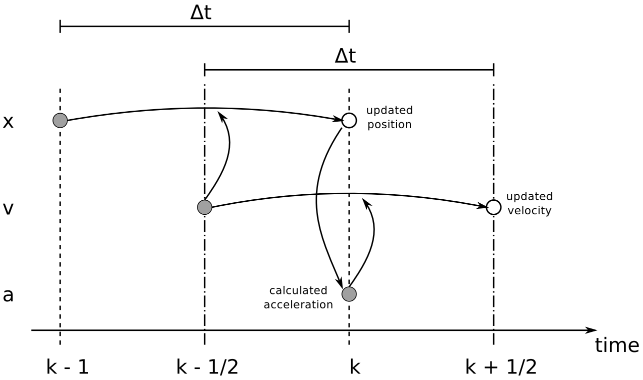

Figure 2.7: Illustration of leapfrog integration algorithm. Positions and velocities are calculated at different times.

be calculated as follows:

$$\vec{x}_i^k = \vec{x}_i^{k-1} + \vec{v}_i^{k-1/2}\Delta t \tag{2.13}$$

$$\vec{a}_i^k = \frac{1}{m_i}\sum_{j\neq i}^{N} \vec{F}_{ij}\left(\vec{x}_i^k - \vec{x}_j^k\right) \tag{2.14}$$

$$\vec{v}_i^{k+1/2} = \vec{v}_i^{k-1/2} + \vec{a}_i^k\Delta t \tag{2.15}$$

The first equation yields the new position at time k, using the position in the previous time-step $k-1$ and the velocity half step before, i.e. $k-1/2$; the updated positions $\vec{x}_i^k$ are then used in equation 2.14, to calculate the acceleration of each particle at the same time k. Finally the acceleration is used to propagate velocities by one time-step, obtaining the new velocities at time $k+1/2$. The procedure is illustrated in figure 2.7. It can be observed from the illustration that while positions and accelerations are calculated at the same time, velocities are given always half a step ahead, and it seems that positions and velocities are always jumping in front of each other in the time line, hence the name *leapfrog*. Despite this algorithm's accuracy is only $\mathcal{O}\left(\Delta t^2\right)$ (second order in Δt), it was chosen for our implementation over more accurate higher order methods such as Runge-Kutta or Predictor-Corrector. The main reason for this choice is the extreme simplicity of implementation of the leapfrog algorithm, combined to its speed. Furthermore, this algorithms shows excellent stability i.e. it conserves energy, it is reversible and while the particle's positions are integrated with an accuracy of $\mathcal{O}\left(\Delta t^2\right)$, the square of Δt is never calculated explicitly, improving the numerical stability. Leapfrog is a common choice among MD simulation software, and its accuracy is more than enough to reproduce statistical properties of conventional systems correctly.

The equations of motion 2.12 describe a Newtonian system, where the total energy is conserved, but often it is more relevant to simulate a system where the overall temperature is constant, or fluctuating around a set-point value, thus reproducing the behaviour of a canonical ensemble. According to the kinetic theory, the temperature of the system can be calculated from the kinematic properties of the particles as follows:

$$T = \frac{2}{3Nk_B} \sum_i^N \frac{1}{2} m_i v_i^2 \tag{2.16}$$

therefore, it is possible to control the temperature by modifying the velocity of the particles. There are different ways to simulate the coupling of the system with a heat bath, depending on how velocities are rescaled during the simulation [79, 80, 81].

Notice that since this is a classical problem, it is chaotic, i.e. the behaviour of the system depends critically on the initial conditions, which are in principle unknown. Positions are normally chosen in the beginning so that particles should not be too close to each other but regarding velocities, all we can do is choose some that respect certain criteria: most often the initial velocities are randomly drawn from the Maxwell-Boltzmann distribution for the desired temperature. Then the system is equilibrated for a while so that both positions and velocities represent a valid microstate of the system. Still, from this point the system can evolve in only one possible way, and if the process we hope to see is stochastic, it might never occur in the simulation. For this reason, the same MD simulation should be performed several times, starting from a different microstate to gather statistics.

2.4.2 Modelling the Oscillation

While the motion of every atom is integrated, the tip needs to oscillate as it would in a real NC-AFM experiment. To simulate the conventional FM-AFM mode, we just impose an harmonic motion in the vertical direction to the atomic holders of the tip; the frequency of this oscillation is typically about 150 kHz, leading to a total simulation time of about 6 μs. If we use a time-step of 1 fs, this means integrating 6 billions steps, and the simulation would take months. For this reason we speed up the oscillation to 150 MHz, which is 3 orders of magnitude faster than the real thing, but it is still way below the THz regime of atomic vibrations; with this we assume that the dissipative processes we are looking for, happen on a faster time-scale, namely picoseconds, and the increased frequency in the simulation does not yield any statistical change. Of course, this is just an approximation, but our tests showed no visible change in the behaviour of the system below 500 MHz. Another way to reduce the simulation time is to ignore the upper part of the tip oscillation: this can be done if the tip is far enough from the surface, thus their interaction is too weak to trigger conformational changes responsible for hysteresis (figure 2.8). The portion of the loop that can be cut out depends on the effective range

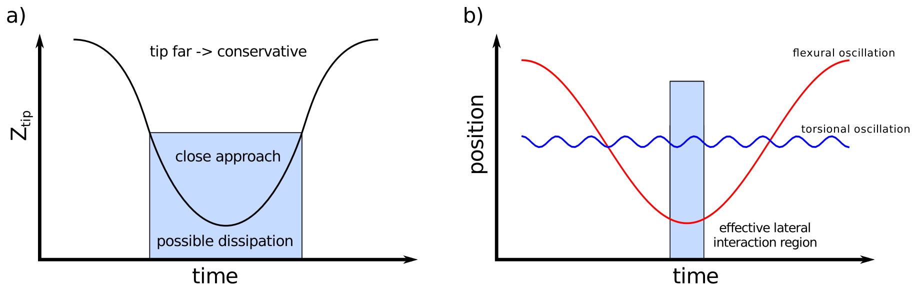

Figure 2.8: (a) In FM-AFM, only part of the loop might be enough to see dissipative processes as they are unlikely to occur when the tip is far from the surface. (b) Lateral dissipative processes in bimodal mode are simulated by constant height lateral cycles, in the small region where the tip is close enough to the surface. During the remaining time, lateral forces are negligible and do not give dissipation.

of dissipative processes, the oscillation amplitude and the tip-sample distance. TR-AFM cycles can be simulated in the same way, just by making the oscillation parallel to the surface, but if torsional and flexural modes are combined in bimodal AFM, then a more elaborate scheme is required.

We are also interested in understanding lateral dissipation processes, as experimentally observed using bimodal AFM. In this case, the tip position at any time can be calculated as:

$$A_z \cos\left(2\pi f_z t\right) \hat{z} + A_y \cos\left(2\pi f_y t\right) \hat{y} \tag{2.17}$$

where A_z, A_y are the amplitudes, f_z, f_y the frequencies and $\hat{z}$, $\hat{y}$ the directions of the flexural and torsional oscillations respectively. According to the experimental setup, the torsional frequency f_y is roughly 10 times higher than f_z and A_y is roughly 10 times smaller than A_z. Performing MD for the full trajectory is not feasible, as one oscillation will be too fast, going outside of the boundaries of our assumptions explained earlier, although, we can efficiently simulate an oscillation cycle in the lateral direction, at constant height and f_y of 150 MHz. If we look carefully at the tip's trajectory in equation 2.17, with the experimental values for amplitude and frequencies, we find out that while the tip is at the lower turning point of the flexural cycle, it spends there enough time to complete almost one full lateral oscillation, before retracting further away from the surface where lateral interactions are considerably smaller. Moreover, the two frequencies f_z and f_y are incommensurate, thus, at every vertical approach, the phase of the lateral oscillation is different. Afterwards, the tip spends most of the oscillation period far from the surface, where it has enough time to erase memory of any structural changes in the apex. The correct way to proceed is then to run MD simulations for a certain portion of the torsional cycle repeatedly, making sure that each time the tip starts the oscillation with a different phase, and from its relaxed configuration. After averaging the forward and backward sweeps extracted from the partial loops, the hysteresis of the average loop gives the theoretical value of energy dissipation, calculated at constant height. The lateral energy dissipation in bimodal mode can be calculated considering that for each torsional cycle occurring close to the surface - the one we simulate -, due to the frequency difference, the other 9 cycles occur far from the surface, where we assume lateral forces to be vanishing and dissipation is zero. The dissipation signal coming from the experimental apparatus is already an average over several thousands cycles, at all heights swept by the flexural oscillation.

2.4.3 GPU Implementation

When calculating the dynamics of a finite-size system, with no periodic boundary conditions, the computational cost of the evaluation of interatomic forces in expression 2.14 requires all the $\mathcal{O}\left(N^2\right)$ operations and is the bottleneck of our calculation. Cutting off the interaction would give a large error because of the long range Coulomb forces, therefore, we cannot make use of computational tricks such as neighbour lists and domain decomposition to improve the scaling. Multipole methods had been implemented before, but their speedup becomes relevant only for very large systems, and this is indeed not our case. The other main issue comes from the need to repeat the same calculation several times with different starting conditions, in order to get a statistical sample large enough to extract meaningful average values, namely tip-sample forces and energy dissipation. Using a different kind of computer architecture we managed to address both problems at the same time.

Fortunately, the evaluation of interatomic forces can be trivially calculated in a parallel fashion, since the calculation for one particular atom, does not depend on the result obtained on another atoms: each one can be processed separately and concurrently. Such a problem is very well suited for the novel general purpose graphic processing units (GP-GPUs) [82, 83, 84], which can bring Teraflop computing power in a simple desktop computer. This architecture was originally intended to provide appealing 3D graphics to entertainment applications, where a list (or stream) of vertexes describing geometrical shapes, defines the input for a small and simple *shader* program; the shader computes how light interact with the surface of the object in each particular vertex and returns a colour value in a given position on the screen. As the market's demands increased, manufacturers were pushed to fit larger amounts of processors on the GPU, in order to process more detailed geometries with more elaborate shader programs. Modern GPUs typically feature more than 500 streaming multiprocessors (SMs), each capable of executing the same instruction for 32 threads, and despite that the speed of a single core is much lower than the speed of a conventional CPU ($\sim$ 3 GHz), the massive amount of concurrent threads being executed at a time, largely compensate for it. GPUs were successfully

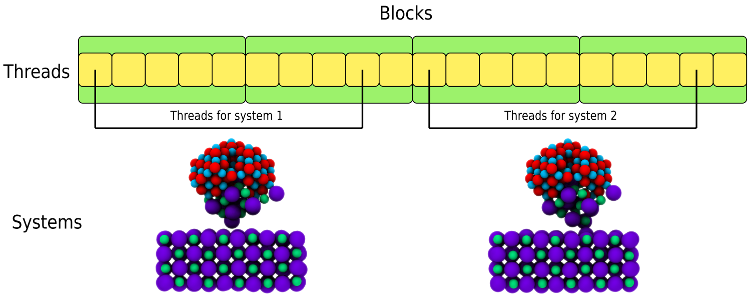

Figure 2.9: Multiple copies of the system are computed concurrently.

programmed to solve particle based problems, such as collision detection [85] and rigid body dynamics [86], proving their scientific computing capability. The drawback is that writing an efficient program for GPU architectures is not an easy task, and even for a skilled programmer, obtaining better performance than a normal CPU implementation is not trivial: knowledge of the hardware details is required in order to squeeze every drop of performance out of a GPU.

An efficient way to evaluate all-pairs interactions was suggested in Ref.[87], and we based our implementation along the same lines. This way we can already obtain a good performance improvement over the CPU code, however it is not as good as expected, and there are two main issues involved. First of all, our system consists roughly of 600 atoms so that few stream processors are needed to compute our system, while most of them are not doing anything at all. Secondly, all the $\mathcal{O}(N)$ operations, such as position and speed updates, take more time in memory access than actual computation and they happen to be even slower than their CPU equivalent. To fill all the computational resources, we stacked multiple copies of the same system in the GPU memory and mapped the threads to the atoms as illustrated in figure 2.9. For each copy, the atomic velocities are initialised with different random values from a Maxwell-Boltzmann distribution, thus the simulation provides different possible trajectories at the same time. By computing 20 copies of the system we increased our speed-up factor by almost as much.

Better performance is possible by computing everything using single precision numbers (32 bits representation) instead of double precision (64 bits), especially on older GPUs, where the double precision arithmetical processors are considerably less abundant than the single precision ones. By doing so, further care needs to be taken, as the effects of error propagation started to appear.

3

Applications

In the following sections we summarise the main results of our efforts, going through the different research projects where the theoretical methods explained in chapter 2 were directly applied.

3.1 High Resolution Imaging of the $MgAl_2O_4$ Spinel Surface

The $MgAl_2O_4$ spinel surface was extensively studied throughout papers II, III and VI using NC-AFM and theoretical calculations. Two different kind of contrast were experimentally obtained on the clean surface (figure 3.1), both showing atomic scale features, but none matching the previously predicted Mg termination; the images also revealed the presence of defects on the surface. In order to understand the imaging mechanism, and ultimately the surface termination and type of defects seen in the NC-AFM images, we carried out several theoretical calculations. The energy of different surface terminations was calculated with DFT, taking into account the partial oxygen pressure and temperature at which the samples were prepared, taking into account thermodynamic energy contributions. Our first results pointed out that the O_4-Al_4-O_4 termination was energetically more favourable than the Mg one, only when inversion defect and hydrogen are present on the surface; other kind of defects such as O or Al vacancies have too high formation energy, and are thus unlikely to appear.

Using a simple MgO cubic tip model, we calculated the interaction forcefield for the O_4-Al_4-O_4 surface termination, gradually including inversion defects and eventually hydrogen, in different densities, to be used in our virtual-AFM: due to the computational cost of DFT, few force-distance curves were computed on the most relevant positions above the unit cell, and then, exploiting the symmetries of the surface, extrapolated on a fine regular grid for the simulation package. Both imaging contrasts were reproduced depending on the tip termination: a negative (O) terminated tip interacted strongly with the Al atoms, revealing their row-like structure, while the positively (Mg) terminated

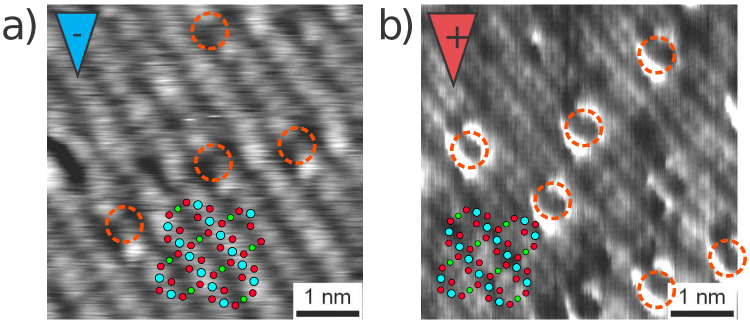

Figure 3.1: Atomically resolved NC-AFM images measured with a negative (a) and positive (b) tip termination with inversion defects marked by dashed circles. The overlaid ball model indicates the position of Al (cyan), O (red) and subsurface Mg (green) atoms. The correct alignment of the ball model was possible by comparing these images with the simulation.

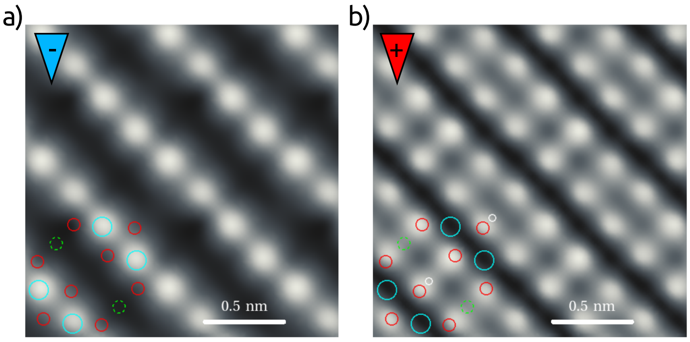

Figure 3.2: Simulated NC-AFM images on the ideal O$_4$-Al$_4$-O$_4$ termination using a negative (a) and positive (b) tip apex.

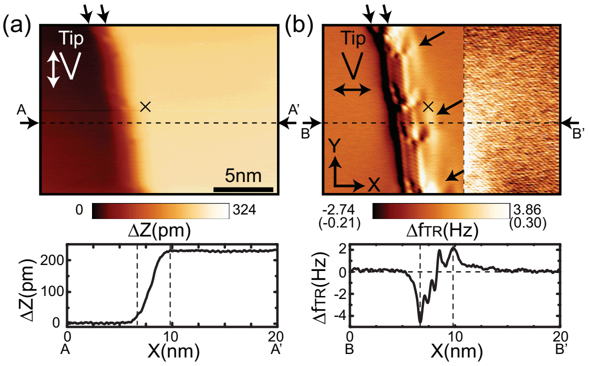

Figure 3.3: Simultaneous topography (a), and torsional frequency shift (b) measured with bimodal AFM on a LiF step edge. The enhanced contrast region in (b) shows the presence of a slowly decaying interaction with the step.

tip showed the double O rows instead. The simulated images were in good qualitative agreement with the real measurements, explaining imaging mechanism on the defect-free regions of the surface (figure 3.2); the apparent asymmetry in O atoms along the rows could also be simulated, and it was possible to relate it to the presence of H adsorbed on the surface. The key characteristics of the inversion defects surrounded by H atoms were captured as well by our model.

3.2 LiF (001) Atomic Step Features

In paper V we investigated interactions of the tip with a LiF (001) atomic step edge using bimodal AFM. The torsional frequency shift Δf_{TR} picked up a long range interaction tail decaying slowly away from the edge on the upper terrace; the flexural Δf_z channel, despite being operated at very small amplitude, could only detect the site-independent van der Waals interaction (figure 3.3). This feature was further investigated applying a bias voltage V between the tip and the bottom on the LiF crystal: while Δf_z showed a quadratic dependence on V as expected, Δf_{TR} changed linearly with V (figure 3.5a,b). The long range feature and this linear dependence on V could not be easily related to atomic scale configurations of the surface, thus we performed a series of theoretical calculations with the idea of simulating the bimodal experiment in our virtual-AFM. In order to take into account the electric polarization of the thick LiF sample, and at the same time, the atomic scale detail of the tip-sample interaction near the step edge, we built a true multiscale model of the system. First a macroscopic model including the sample, the tip and the vacuum chamber was used to calculate the electrostatic potential near the surface using finite element methods [88] (figure 3.3a): the potential there is scaled down with respect to the applied bias at the electrodes, as a result of the

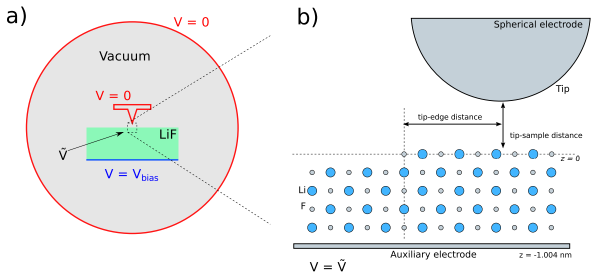

Figure 3.4: (a) Macroscopic model featuring the cantilever-tip assembly, the thick LiF sample and the vacuum chamber. (b) Atomistic model of the step edge.

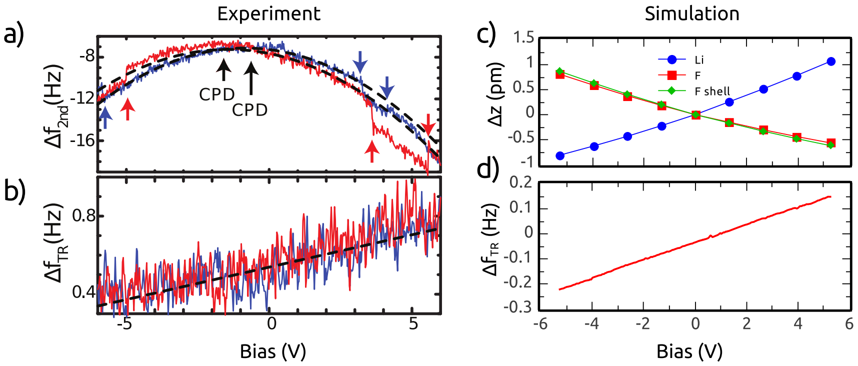

Figure 3.5: Experimentally measured bias dependence of flexural (a) and torsional (b) frequency shifts. (c) Calculated atomic displacements and (d) resulting torsional frequency shift simulated with the virtual-AFM

polarization of the LiF sample. The resulting potential was applied between the tip and a surface electrode in a much smaller atomistic model of the step (figure 3.3b), in order to recreate the electric field on the atoms in that region; the atoms are treated with the shell model and interact through classical pair potentials. The monoatomic step is then relaxed at different tip positions and bias voltages; the effect of the electric field on the step atoms resulted in an almost vertical linear displacement of the different atomic species of roughly one picometer. The interaction between the surface dipole and the tip, assumed to be a fixed dipole, provided a 4D forcefield for our virtual-AFM which simulated the bimodal experiment, giving the same Δf_{TR} bias dependence as observed.

We concluded that site-dependent long-range interactions, despite being hidden by site-dependent forces in the flexural channel, give a distinguishable signature in the torsional channel, as it is insensitive to site-independent interactions. With the combination of experiments and simulations, we could determine that picometer displacements of step atoms were responsible for the long-range interaction detected by Δf_{TR}, demonstrating its extreme sensitivity.

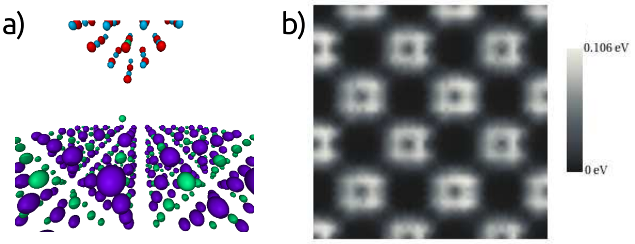

Figure 3.6: (a) The dissipative process is modelled as a surface Na atom jumping stochastically towards the tip. (b) Dissipation image calculated with the virtual-AFM.

3.3 NC-AFM Dissipative Processes on NaCl (001) Surface

In the following sections we present the main results of our investigation of NC-AFM dissipative processes on the NaCl surface, using both the quasi-static method described in section 2.3, and the more advanced molecular dynamics approach introduced in section 2.4.

3.3.1 Quasi-static Method

In paper I, we studied NC-AFM dissipative processes in the ionic crystal surface, taking NaCl (001) as template, within the framework of theory of dynamic response introduced in section 2.3; the goal of this work was to understand the characteristics required of the tip in order to activate dissipative processes, modelled as a bistability of the surface. For this kind of system, interatomic interactions were treated classically, using the shell model [68] and simple Buckingham pairwise potentials [69]. The forcefield and the dissipative field were calculated for a variety of tips obtained from ideal ionic crystals such as NaCl, KBr and MgO, introducing progressively more stoichiometric and structural defects. Ideal tips, regardless of their material, did not perturb the surface enough for a second stable state to arise: this was associated with their high stability. It was possible to model a tip such that a surface atom could find a secondary stable state B when displaced towards the apex, however, due to the limitation of static calculations, this state was effectively the global energy minimum of the system, causing the tip to absorb the surface atom and change permanently. This mechanism is often observed in experimental works, when the imaging contrast suddenly changes during the scan. A stable tip that gave the desired states was found by introducing a substitutional Na impurity in an MgO tip, effectively adding one electronic charge to it; the force and dissipative fields were fed to our virtual-AFM that simulated an NC-AFM experiment, and dissipation comparable to typical experimental values was predicted. Despite

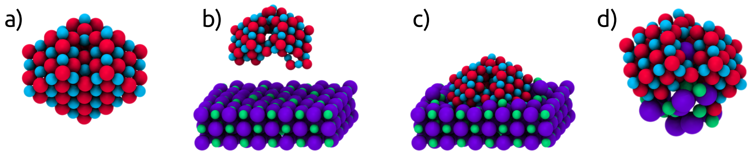

Figure 3.7: Phases of the tip construction. (a) We start from the ideal MgO cubic tip, and (b) make the apex rough. (c) The resulting tip is pushed into a NaCl clean surface and (d) a NaCl nanocluster adsorbs to the apex.

the difficulties and the issues related with the model, this work pointed out that while the frequency shift contrast is mostly sensitive to the foremost atom in the tip apex, there is a strong dependence of the dissipation on a wider range of tip properties.

3.3.2 Dynamical Simulations

We investigated the atomic scale nature of dissipative processes on the NaCl (001) flat surface, using experimental measurements of static (SFS) and dynamic force spectroscopy (DFS) provided by our collaborators from University of Basel, and our newly developed MD software (see section 2.4), aiming at characterising NC-AFM dissipative processes. This work was published in paper IV. Different series of force-distance curves collected using SFS showed similar values for each approach curve, but the retraction curves were never reproducible: in most instances there was no clear difference between the two, although in a few cases a large hysteresis could be observed. This suggests that the tip and the surface do not degrade while the measurements are performed, but the shape of the curves hinted at the formation of atomic chains upon retraction. Unfortunately this kind of measurement is quite noisy and, in the distance regime of NC-AFM, the dissipative process could not be clearly seen, nor attributable to the formation of atomic chains: this was of no help in understanding the energy dissipation measured with DFS. In our initial MD simulations we modelled the tip from an ideal NaCl cubic cluster, similar to the ones explained in the previous section, hoping that including the finite temperature effects of atomic vibrations could show different processes. As a matter of fact we recovered the same result as the quasi-static method: the ideal tip is too stable and no dissipation was seen. A more realistic tip model was obtained using MD to fabricate the tip by indenting an MgO rough cluster in a thick NaCl slab; some of the surface atoms were adsorbed by the oxide and formed an amorphous nanocluster at the apex (figure 3.7). The oscillation cycles simulated with this tip showed how a few atoms from the apex tend to jump towards the surface as the tip approaches, and upon retraction other atoms diffuse from the tip and form an atomic chain. Most of the chains are

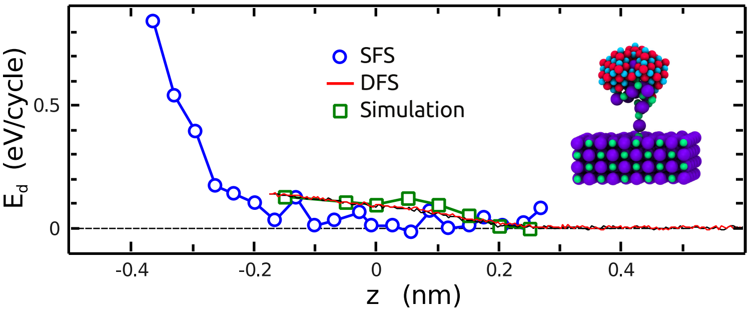

Figure 3.8: Energy dissipation obtained from DFS measurement (red line), average SFS hysteresis (blue circles), and MD simulation (green squares). The inset shows a snapshot from the MD trajectory where a long atomic chain diffused to the tip.

shorter than 0.2 nm giving an hysteresis of about 0.1 eV. Rarely the chains can be 1 nm long with hysteresis of 0.7 eV, however, most of the loops have almost zero hysteresis as no dramatic atomic displacement occurs during the cycle. After averaging hundreds of such cycles, calculated at different tip-sample distances, we obtain the distance dependence dissipation in good agreement with the experimental DFS measurement (figure 3.8).

One important issue we encountered was the degradation of the tip in our simulations: due to the small size of the NaCl nanocluster, if a long chain is pulled, it can easily reconstruct to a more stable configuration when it breaks and diffuses back to the tip. The apex, despite still being much softer, resembles the perfect NaCl crystalline tip, and the dissipation mechanism is hampered. Furthermore, we noticed that the simulated forces are smaller than the ones extracted from the experimental data, suggesting that the simulated tip is smaller than the real one, giving an overall weaker interaction.

Another interesting result was obtained with bimodal AFM on a flat NaCl:Br (001) surface; even though the original aim of the measurements was to prove how the torsional oscillation could be operated easily at very small amplitudes, ensuring greater sensitivity and resolution than the flexural mode, the experimentalists were puzzled by the peculiar pattern of lateral dissipation images, which is related to the frictional properties of the surface. The flexural frequency shift Δf_z gave images where the atomic pattern could be observed with a few Hz contrast (figure 3.9a), while the same pattern was more sharply defined in the torsional frequency shift Δf_{TR} maps, with a much higher contrast of about 20 Hz (figure 3.9b); the atomic pattern was barely visible in the flexural dissipation images, although the noise is too high. The lateral dissipation E_{TR} images showed a different kind of pattern (figure 3.9c), where a certain atomic species appears with two bright dissipation spots on its sides. More importantly, some of these features appear brighter, suggesting that these correspond to the Br defects known to be on the surface.

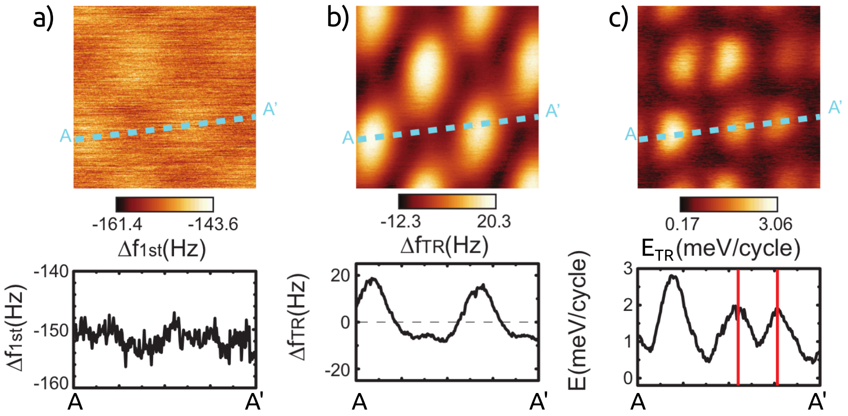

Figure 3.9: (a) Constant height flexural frequency shift, (b) torsional frequency shift, and (c) torsional dissipation maps simultaneously measured with bimodal AFM on a flat NaCl:Br surface.

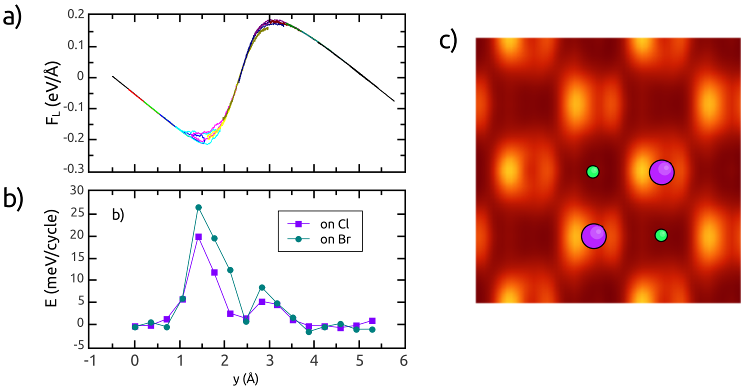

Figure 3.10: (a) Simulated lateral force curves, with (b) their average dissipation along an atomic line with either Cl or Br impurity. (c) Simulated lateral dissipation image.

Our first guess was that the weird E_{TR} pattern was caused by the vertical dissipation processes with the influence of the torsional oscillation inducing imaging artefacts. At first we tried to operate the virtual-AFM in bimodal mode, using the same forcefield and dissipative fields calculated previously, but this approach was unsuccessful and no lateral dissipation could be calculated. Combined with the fact that no remarkable flexural dissipation was measured, all the measurements point out the existence of a different dissipative process, characterised by the lateral tip-surface interaction.

We simulated the bimodal oscillation with our MD program as explained in section 2.4.2, using the reconstructed tip from the previous calculations. It is already known that the chain formation responsible for flexural dissipation is unfavoured with this tip, and the sharp Cl termination explains the Δf_z images. The calculated atomic trajectories showed how small and reversible reconstructions can happen in the apex, depending on the lateral position of the tip during the oscillation. We found out that these reconstructions are more likely to occur when the apex feels a strong repulsive lateral force, and this happens to be the case when the tip is adjacent to a surface Cl or Br atom. The simulated dissipation scanline and image showed the same pattern observed in the experiments, with a very good quantitative agreement (figure 3.10). The dissipation on Br impurities was higher than on Cl, and this could be related to the slightly higher tip-Br repulsion and the localised surface softness around the defect.

Paper VII showing these results is currently in preparation.

4
Conclusions

4.1 Summary

The studies that led to this thesis include the development of methods and simulation software, and their application to specific study cases. The combined experimental techniques and theoretical calculations, made it possible in paper II to identify the $MgAl_2O_4$ spinel surface, which is an important oxide material for catalytic applications. We were able to distinguish the experimental patterns and relate them to the termination of the tip apex; the characteristic features of inversion defects (paper III) and adsorbed H atoms (paper VI) could also be understood from the comparison of simulated images of different configurations of the surface. In paper V we focused on a LiF step edge, using bimodal AFM measurements and multiscale modelling techniques. The vertical signals are sensitive to site-independent interactions such as van der Waals, which hide the long-range features of the step edge; these interactions are symmetric with respect to a direction parallel to the surface plane, hence they do not influence the torsional oscillation. The torsional frequency shift trend in bias dependent dynamic force spectroscopy could be explained by our model as originating from picometer displacement of step atoms in the presence of an electric field. This proved the extreme sensitivity of the torsional channel to site-dependent interactions. The fundamental question of NC-AFM energy dissipation in ionic crystal surfaces was addressed from a purely theoretical point of view in paper I, with the extensive application of the theory of dynamic response; the important result obtained was that the tip plays a major role in the observed dissipation, and we could explain the characteristics required to the tip in order to trigger the dissipative processes in the surface. The limitations of the quasi-static method made it difficult to find a *proper* tip for dissipation, and actually impossible to foresee and include different kind of processes. Some of these limiting barriers were lifted with the implementation of a full dynamical simulation code, able to calculate the behaviour of the system from the trajectories of the individual atoms during the NC-AFM oscillation cycles on a flat NaCl (001) surface. From these molecular dynamics calculations we first found one of the results of the quasi-static approach: ideal tips are too stable and no dissipative process arise. Using a more realistic tip model, created dynamically, we could see how the stochastic formation and rupture of atomic chains is effectively the main process responsible for dissipation and, after averaging hundreds of trajectories, we obtained values in good agreement with the experiments reported in paper IV. The same approach was used to investigate dissipative processes in the torsional oscillation, giving interesting insight into the frictional properties of the surface. Our simulations showed how small apex reconstructions are triggered by strong repulsive interactions with the surface; the tip-sample force reaches its maxima in the region around surface Cl or Br atoms, where the stochastic reconstruction is more frequency and dissipation arise. The calculated lateral dissipation image displayed the same pattern obtained experimentally, with good quantitative agreement.

4.2 Perspective

Even though the original idea of AFM was to measure the surface potential, and ultimately its atomic structure, through the interaction with a probe, the probe itself is not a *silent* partner but plays a role that is sometimes difficult to evaluate. The interaction strongly depends on the atomic scale details of the tip apex and dissipative processes can even involve more than just the few foremost atoms: this is quite an issue since there is no such information available from the experiment. Moreover, the interaction with the surface often causes the tip to change over time and the experiments become harder to reproduce. For these reasons, efforts are being made in the NC-AFM community to fabricate tips with a well defined termination, for example by adsorbing a small molecule at the apex through manipulation [89, 90], although its mobility is still problematic for room temperature applications. The issue of the tip presents itself in theoretical calculations aimed to predict the outcome of a NC-AFM experiment, and often a great deal of time is spent looking for the *right* tip that matches the observations on simple, well known surfaces. However, once this tip is found, the features shown in the experimental images can be understood and related to physical processes happening in the system at the atomic scale, ultimately pointing the NC-AFM field towards a more tip-independent direction. Despite the successes of the theoretical models, with the joint efforts of our experimental collaborators, more work is necessary to extend our models towards larger scales, in order to provide better understanding of more complex materials and processes. Our work in the field of energy dissipation proves the importance of a full dynamical simulation to reveal the different dissipative processes and the efforts spent in developing a fast GPU implementation allowed us to calculate longer trajectories and gather statistics at the same time, which is of central importance. Future work can be done to implement more complex interaction schemes and extend this kind of studies to different systems.

Bibliography

[1] G. Binnig, C. F. Quate, and C. Gerber, Atomic Force Microscope, *Physical Review Letters*, **56**, 930, 1986

[2] Y. Martin, C. C. Williams, and H. K. Wickramasinghe, Atomic force microscope-force mapping and profiling on a sub 100-Å scale, *Journal of Applied Physics*, **61**, 4723, 1987

[3] B. Anczykowski, D. Krüger, and H. Fuchs, Cantilever dynamics in quasi-noncontact force microscopy: Spectroscopic aspects, *Physical Review B*, **53**, 15485, 1996

[4] A. Schirmeisen, H. Hölscher, B. Anczykowski, D. Weiner, M. M. Schäfer, and H. Fuchs, Dynamic force spectroscopy using the constant-excitation and constant-amplitude modes, *Nanotechnology*, **16**, S13, 2005

[5] T. R. Albrecht, P. Grütter, D. Horne, and D. Rugar, Frequency modulation detection using high-Q cantilevers for enhanced force microscope sensitivity, *Journal of Applied Physics*, **69**, 668, 1991

[6] F. J. Giessibl, Atomic Resolution of the Silicon (111)-(7x7) Surface by Atomic Force Microscopy, *Science*, **267**, 68, 1995

[7] M. Bammerlin, R. Luthi, E. Meyer, A. Barato, J. Lu, M. Guggisberg, C. Gerber, L. Howald, and H. J. Guntherodt, True Atomic Resolution on the Surface of an Insulator via Ultrahigh Vacuum Dynamic Force Microscopy, *Probe Microscopy*, **1**, 3, 1997

[8] C. Barth and M. Reichling, Imaging the atomic arrangements on the high-temperature reconstructed -Al_2O_3(0001) surface, *Nature*, **414**, 54, 2001

[9] Y. Sugawara, M. Ohta, H. Ueyama, and S. Morita, Defect Motion on an InP(110) Surface Observed with Noncontact Atomic Force Microscopy, *Science*, **270**, 1646, 1995

[10] T. Fukuma, M. Kimura, K. Kobayashi, K. Matsuhige, and H. Yamada, Development of low noise cantilever deflection sensor for multienvironment frequency-modulation atomic force microscopy, *Review of Scientific Instruments*, **76**, 053704, 2005

[11] T. Fukuma, K. Kobayashi, K. Matsushige, and H. Yamada, True molecular resolution in liquid by frequency-modulation atomic force microscopy, *Applied Physics Letters*, **86**(19), 193108, 2005

[12] T. Fukuma, T. Ichii, K. Kobayashi, H. Yamada, and K. Matsushige, True-molecular resolution imaging by frequency modulation atomic force microscopy in various environments, *Applied Physics Letters*, **86**(3), 034103, 2005

[13] S. Rode, N. Oyabu, K. Kobayashi, H. Yamada, and A. Kühnle, True Atomic-Resolution Imaging of $(10\bar{1}4)$ Calcite in Aqueous Solution by Frequency Modulation Atomic Force Microscopy, *Langmuir*, **25**(5), 2850, 2009

[14] H. Yamada, T. Fukuma, K. Umeda, K. Kobayashi, and K. Matsushige, Local structures and electrical properties of organic molecular films investigated by non-contact atomic force microscopy, *Applied Surface Science*, **188**, 391, 2002

[15] F. J. Giessibl, Forces and frequency shifts in atomic-resolution dynamic-force microscopy, *Physical Review B*, **56**, 16010, 1997

[16] H. Hölscher, W. Allers, U. D. Schwarz, A. Schwarz, and R. Wiesendanger, Determination of Tip-Sample Interaction Potentials by Dynamic Force Spectroscopy, *Physical Review Letters*, **83**, 4780, 1999

[17] U. Dürig, Relations between interaction force and frequency shift in large-amplitude dynamic force microscopy, *Applied Physics Letters*, **75**, 433, 1999

[18] Y. Martin and H. K. Wickramasinghe, Magnetic imaging by “force microscopy” with 1000 [Å-ring] resolution, *Applied Physics Letters*, **50**(20), 1455, 1987

[19] M. Nonnenmacher, M. P. O’Boyle, and H. K. Wickramasinghe, Kelvin probe force microscopy, *Applied Physics Letters*, **58**(25), 2921, 1991

[20] C. Loppacher, U. Zerweck, S. Teich, E. Beyreuther, T. Otto, S. Grafström, and L. Eng, FM demodulated Kelvin probe force microscopy for surface photovoltage tracking, *Nanotechnology*, **16**, S1, 2005

[21] C. Barth and C. R. Henry, Kelvin probe force microscopy on surfaces of UHV cleaved ionic crystals, *Nanotechnology*, **17**, S155, 2006

[22] R. Overney, E. Meyer, J. Frommer, D. Brodbeck, R. Lüthi, L. Howald, H. J. Güntherodt, M. Fujihira, H. Takano, and Y. Gotoh, Friction measurements on phase-separated thin films with a modified atomic force microscope, *Nature*, **359**, 133, 1992

[23] E. Meyer, R. Lüthi, L. Howald, M. Bammerlin, M. Guggisberg, and H.-J. Güntherodt, Site-specific friction force spectroscopy, *Journal of Vacuum Science & Technology B*, **14**, 1285, 1996

[24] T. Müller, M. Lohrmann, T. Kässer, O. Mart, , J. Mlynek, and G. Krausch, Frictional Force between a Sharp Asperity and a Surface Step, *Physical Review Letters*, **79**, 5066, 1997

[25] E. Gnecco, R. Bennewitz, T. Gyalog, C. Loppacher, M. Bammerlin, E. Meyer, and H. J. Guntherodt, Velocity Dependence of Atomic Friction, *Physical Review Letters*, **84**, 1172, 2000

[26] A. Socoliuc, R. Bennewitz, E. Gnecco, and E. Meyer, Transition from Stick-Slip to Continuous Sliding in Atomic Friction: Entering a New Regime of Ultralow Friction, *Physical Review Letters*, **92**, 134301, 2004

[27] E. Meyer, R. Overney, D. Brodbeck, L. Howald, R. Lüthi, J. Frommer, and H. J. Güntherodt, Friction and wear of Langmuir-Blodgett films observed by friction force microscopy, *Physical Review Letters*, **69**, 1777, 1992

[28] E. Gnecco, R. Bennewitz, and E. Meyer, Abrasive Wear on the Atomic Scale, *Physical Review Letters*, **88**, 215501, 2002

[29] B. Gotsmann and M. A. Lantz, Atomistic Wear in a Single Asperity Sliding Contact, *Physical Review Letters*, **101**, 125501, 2008

[30] T. Kawagishi, A. Kato, Y. Hoshi, and H. Kawakatsu, Mapping of lateral vibration of the tip in atomic force microscopy at the torsional resonance of the cantilever, *Ultramicroscopy*, **91**, 37, 2002

[31] M. Reinstädtler, U. Rabe, V. Scherer, and U. Hartmann, On the nanoscale measurement of friction using atomic-force microscope cantilever torsional resonances, *Applied Physics Letters*, **82**, 2604, 2003

[32] S. Kawai, T. Glatzel, S. Koch, B. Such, A. Baratoff, and E. Meyer, Ultrasensitive detection of lateral atomic-scale interactions on graphite (0001) via bimodal dynamic force measurements, *Physical Review B*, **81**, 085420, 2010

[33] G. Malegori and G. Ferrini, Wavelet transforms to probe long- and short-range forces by thermally excited dynamic force spectroscopy, *Nanotechnology*, **22**(19), 195702, 2011

[34] D. Kobayashi, S. Kawai, and H. Kawakatsu, New FM Detection Techniques for Scanning Probe Microscopy, *Japanese Journal of Applied Physics*, **43**, 4566, 2004

[35] A. I. Livshits, A. L. Shluger, A. L. Rohl, and A. S. Foster, Model of noncontact scanning force microscopy on ionic surfaces, *Physical Review B*, **59**, 2436, 1999

[36] U. Dürig, Interaction sensing in dynamic force microscopy, *New Journal of Physics*, **2**, 5, 2000

[37] G. Couturier, J. Aimé, J. Salardenne, and R. Boisgard, A virtual non contact-atomic force microscope (NC-AFM): Simulation and comparison with analytical models, *European Physical Journal-Applied Physics*, **15**(2), 141, 2001

[38] U. Dürig, Extracting interaction forces and complementary observables in dynamic probe microscopy, *Applied Physics Letters*, **76**(9), 1203, 2000

[39] F. J. Giessibl, A direct method to calculate tip-sample forces from frequency shifts in frequency-modulation atomic force microscopy, *Applied Physics Letters*, **78**, 123, 2001

[40] J. E. Sader and S. P. Jarvis, Accurate formulas for interaction force and energy in frequency modulation force spectroscopy, *Applied Physics Letters*, **84**, 1801, 2004

[41] B. Anczykowski, B. Gotsmann, H. Fuchs, J. P. Cleveland, and V. B. Elings, How to measure energy dissipation in dynamic mode atomic force microscopy, *Applied Surface Science*, **140**, 376, 1999

[42] O. Pfeiffer, L. Nony, R. Bennewitz, A. Baratoff, and E. Meyer, Distance dependence of force and dissipation in non-contact atomic force microscopy on Cu(100) and Al(111), *Nanotechnology*, **15**, S101, 2004

[43] H. O. Ozer, S. J. O'Brien, A. Norris, J. E. Sader, and J. B. Pethica, Dissipation imaging with low amplitude off-resonance atomic force microscopy, *Japanese Journal of Applied Physics*, **44**(7B), 5325, 2005

[44] V. Caciuc, H. Hölscher, D. Weiner, H. Fuchs, and A. Schirmeisen, Noncontact atomic force microscopy imaging mechanism on Ag(110): Experiment and first-principles theory, *Physical Review B*, **77**, 045411, 2008

[45] S. Hembacher, F. J.Giessibl, J. Mannhart, and C. F. Quate, Local Spectroscopy and Atomic Imaging of Tunneling Current, Forces, and Dissipation on Graphite, *Physical Review Letters*, **94**, 056101, 2005

[46] T. Filleter, J. L. McChesney, A. Bostwick, E. Rotenberg, K. V. Emtsev, T. Seyller, K. Horn, and R. Bennewitz, Friction and Dissipation in Epitaxial Graphene Films, *Physical Review Letters*, **102**, 086102, 2009

[47] N. Oyabu, P. Pou, Y. Sugimoto, P. Jelinek, M. Abe, S. Morita, R. Pérez, and O. Custance, Single Atomic Contact Adhesion and Dissipation in Dynamic Force Microscopy, *Physical Review Letters*, **96**, 106101, 2006

[48] H. O. Ozer, M. Atabak, and A. Oral, Measurement of energy dissipation between tungsten tip and Si(100)-(2×1) using sub-ångström oscillation amplitude non-contact atomic force microscope, *Applied Surface Science*, **210**(1-2), 12 , 2003, 5th International Conference on non-contact AFM in Montreal, Canada

[49] S. Maier, O. Pfeiffer, T. Glatzel, E. Meyer, T. Filleter, and R. Bennewitz, Asymmetry in the reciprocal epitaxy of NaCl and KBr, *Physical Review B*, **75**, 195408, 2007

[50] R. Bennewitz, S. Schär, E. Gnecco, O. Pfeiffer, M. Bammerlin, and E. Meyer, Atomic structure of alkali halide surfaces, *Applied Physics A*, **78**, 837, 2004

[51] S. Torbrügge, M. Reichling, A. Ishiyama, S. Morita, and O. Custance, Evidence of Subsurface Oxygen Vacancy Ordering on Reduced CeO_2(111), *Physical Review Letters*, **99**, 056101, 2007

[52] R. Bennewitz, A. S. Foster, L. N. Kantorovich, M. Bammerlin, C. Loppacher, S. Schär, M. Guggisberg, E. Meyer, and A. L. Shluger, Atomically resolved edges and kinks of NaCl islands on Cu(111): Experiment and theory, *Physical Review B*, **62**, 2074, 2000

[53] Y. Seino, S. Yoshikawa, M. Abe, and S. Morita, Growth dynamics of insulating SrF2 films on Si(111), *Journal of Physics: Condensed Matter*, **19**, 445001, 2007

[54] C. Loppacher, R. Bennewitz, O. Pfeiffer, M. Guggisberg, M. Bammerlin, S. Schär, V. Barwich, A. Baratoff, and E. Meyer, Experimental aspects of dissipation force microscopy, *Physical Review B*, **62**, 13674, 2000

[55] R. Hoffmann, A. Baratoff, H. J. Hug, H. R. Hidber, H. v. Löhneysen, and H.-J. Güntherodt, Mechanical manifestations of rare atomic jumps in dynamic force microscopy, *Nanotechnology*, **18**, 395503, 2007

[56] F. J. Giessibl, M. Herz, and J. Mannhart, Friction traced to the single atom, *Proceedings of the National Academy of Sciences of the United States of America*, **99**, 12006, 2002

[57] N. F. Martinez and R. Garcia, Measuring phase shifts and energy dissipation with amplitude modulation atomic force microscopy, *Nanotechnology*, **17**(7), S167, 2006

[58] M. Gauthier and M. Tsukada, Damping Mechanism in Dynamic Force Microscopy, *Physical Review Letters*, **85**, 5348, 2000

[59] M. Gauthier, R. Pérez, T. Arai, M. Tomitori, and M. Tsukada, Interplay between Nonlinearity, Scan Speed, Damping, and Electronics in Frequency Modulation Atomic-Force Microscopy, *Physical Review Letters*, **89**, 146104, 2002

[60] T. Trevethan, L. Kantorovich, J. Polesel-Maris, and S. Gauthier, Is atomic-scale dissipation in NC-AFM real? Investigation using virtual atomic force microscopy, *Nanotechnology*, **18**, 084017, 2007

[61] L. N. Kantorovich, Stochastic friction force mechanism of energy dissipation in noncontact atomic force microscopy, *Physical Review B*, **64**, 245409, 2001

[62] L. N. Kantorovich and T. Trevethan, General Theory of Microscopic Dynamical Response in Surface Probe Microscopy: From Imaging to Dissipation, *Physical Review Letters*, **93**, 236102, 2004

[63] P. Dieska, I. Stich, and R. Pérez, Nanomanipulation Using Only Mechanical Energy, *Physical Review Letters*, **95**(12), 126103, 2005

[64] F. Federici Canova and A. S. Foster, The role of the tip in non-contact atomic force microscopy dissipation images of ionic surfaces, *Nanotechnology*, **22**, 045702, 2011

[65] S. A. Ghasemi, S. Goedecker, A. Baratoff, T. Lenosky, E. Meyer, and H. J. Hug, Ubiquitous Mechanisms of Energy Dissipation in Noncontact Atomic Force Microscopy, *Physical Review Letters*, **100**, 236106, 2008

[66] E. Y. Vedmedenko, Q. Zhu, U. Kaiser, A. Schwarz, and R. Wiesendanger, Atomic-scale magnetic dissipation from spin-dependent adhesion hysteresis, *Physical Review B*, **85**, 174410, 2012

[67] J. Polesel-Maris and S. Gauthier, A virtual dynamic atomic force microscope for image calculations, *Journal of Applied Physics*, **97**, 044902, 2005

[68] B. G. Dick and A. W. Overhauser, Theory of the Dielectric Constants of Alkali Halide Crystals, *Physical Review*, **112**, 90, 1958

[69] R. A. Buckingham, The Classical Equation of State of Gaseous Helium, Neon and Argon, *Proceedings of the Royal Society A*, **168**, 264, 1938

[70] W. Kohn and L. J. Sham, Self-Consistent Equations Including Exchange and Correlation Effects, *Physical Review*, **140**, A1133, 1965

[71] A. L. Shluger, A. L. Rohl, D. H. Gay, and R. T. Williams, Atomistic theory of the interaction between AFM tips and ionic surfaces, *Journal of Physics: Condensed Matter*, **6**, 1825, 1994

[72] P. Hohenberg and W. Kohn, Inhomogeneous Electron Gas, *Physical Review*, **136**, B864, 1964

[73] D. C. Langreth and J. P. Perdew, Theory of nonuniform electronic systems. I. Analysis of the gradient approximation and a generalization that works, *Physical Review B*, **21**, 5469, 1980

[74] D. C. Langreth and M. J. Mehl, Beyond the local-density approximation in calculations of ground-state electronic properties, *Physical Review B*, **28**, 1809, 1983

[75] J. P. Perdew and W. Yue, Accurate and simple density functional for the electronic exchange energy: Generalized gradient approximation, *Physical Review B*, **33**, 8800, 1986

[76] J. P. Perdew, Density-functional approximation for the correlation energy of the inhomogeneous electron gas, *Physical Review B*, **33**, 8822, 1986

[77] A. D. Becke, A new mixing of Hartree–Fock and local density-functional theories, *Journal of Chemical Physics*, **98**(2), 1372, 1993

[78] N. Hine, P. Haynes, A. Mostofi, C.-K. Skylaris, and M. Payne, Linear-scaling density-functional theory with tens of thousands of atoms: Expanding the scope and scale of calculations with ONETEP, *Computer Physics Communications*, **180**(7), 1041 , 2009

[79] H. J. C. Berendsen, J. P. M. Postma, W. F. van Gunsteren, A. DiNola, and J. R. Haak, Molecular dynamics with coupling to an external bath, *Journal of Chemical Physics*, **81**(8), 3684, 1984

[80] S. Nosé, A unified formulation of the constant temperature molecular dynamics methods, *Journal of Chemical Physics*, **81**(1), 511, 1984

[81] W. G. Hoover, Canonical dynamics: Equilibrium phase-space distributions, *Physical Review A*, **31**, 1695, 1985

[82] J. D. Owens, D. Luebke, N. Govindaraju, M. Harris, J. Krüger, A. E. Lefohn, and T. J. Purcell, A Survey of General-Purpose Computation on Graphics Hardware, *Computer Graphics Forum*, **26**(1), 80, 2007

[83] J. D. Owens, M. Houston, D. Luebke, S. Green, J. Stone, and J. Phillips, GPU Computing, *Proceedings of the IEEE*, **96**(5), 879 , 2008

[84] M. Garland, S. L. Grand, J. Nickolls, J. Anderson, J. Hardwick, S. Morton, E. Phillips, Y. Zhang, and V. Volkov, Parallel Computing Experiences with CUDA, *Micro, IEEE*, **28**(4), 13 , 2008

[85] S. Le Grand, *GPU Gems 3: chapter 32*, volume 3, Addison-Wesley Professional, 2007

[86] T. Harada, *GPU Gems 3: chapter 29*, volume 3, Addison-Wesley Professional, 2007

[87] L. Nyland, M. Harris, and J. Prins, *GPU Gems 3: chapter 31*, volume 3, Addison-Wesley Professional, 2007

[88] W. G. Strang and G. J. Fix, *An Analysis of the Finite Element Method*, Prentice-Hall, 1973

[89] L. Gross, F. Mohn, N. Moll, P. Liljeroth, and G. Meyer, The Chemical Structure of a Molecule Resolved by Atomic Force Microscopy, *Science*, **325**, 1110, 2009

[90] Z. Sun, M. P. Boneschanscher, I. Swart, D. Vanmaekelbergh, and P. Liljeroth, Quantitative Atomic Force Microscopy with Carbon Monoxide Terminated Tips, *Physical Review Letters*, **106**, 046104, 2011

5

Publications